

## PROBING THE STRUCTURE AND KINEMATICS OF THE TRANSITION LAYER BETWEEN THE MAGELLANIC STREAM AND THE HALO IN HI

LOU NIGRA<sup>1</sup>, SNEŽANA STANIMIROVIĆ, JOHN S. GALLAGHER, III

Department of Astronomy, University of Wisconsin, 475 North Charter Street, Madison, WI 53706, USA;

KENNETH WOOD<sup>2</sup>

School of Physics and Astronomy, University of St. Andrews, North Haugh, St. Andrews KY16 9SS, UK;

AND

DAVID NIDEVER, STEVEN MAJEWSKI

Department of Astronomy, University of Virginia, Charlottesville, VA, 22904-4325, USA;

*Accepted for publication in The Astrophysical Journal*

### ABSTRACT

The Magellanic Stream (MS) is a nearby laboratory for studying the fate of cool gas streams injected into a gaseous galactic halo. We investigate properties of the boundary layer between the cool MS gas and the hot Milky Way halo with 21 cm HI observations of a relatively isolated cloud having circular projection in the northern MS. Through averaging and modeling techniques, our observations obtained with the Robert C. Byrd Green Bank Telescope (GBT), reach unprecedented  $3\sigma$  sensitivity of  $\sim 1 \times 10^{17} \text{ cm}^{-2}$ , while retaining the telescope's  $9.1'$  resolution in the essential radial dimension. We find an envelope of diffuse neutral gas with FWHM of  $60 \text{ km s}^{-1}$ , associated in velocity with the cloud core having FWHM of  $20 \text{ km s}^{-1}$ , extending to 3.5 times the core radius with a neutral mass seven times that of the core. We show that the envelope is too extended to represent a conduction-dominated layer between the core and the halo. Its observed properties are better explained by a turbulent mixing layer driven by hydrodynamic instabilities. The fortuitous alignment of the NGC 7469 background source near the cloud center allows us to combine UV absorption and HI emission data to determine a core temperature of  $8350 \pm 350 \text{ K}$ . We show that the HI column density and size of the core can be reproduced when a slightly larger cloud is exposed to Galactic and extragalactic background ionizing radiation. Cooling in the large diffuse turbulent mixing layer envelope extends the cloud lifetime by at least a factor of two relative to a simple hydrodynamic ablation case, suggesting that the cloud is likely to reach the Milky Way disk.

*Subject headings:* ISM:clouds — ISM:kinematics and dynamics — ISM:structure — methods:data analysis — turbulence

### 1. INTRODUCTION

The Magellanic Stream (MS) is our closest and most prominent example of a gaseous interaction remnant. While such circumgalactic structures are postulated to represent important sources of fuel for future star formation (Kereš et al. 2005; Wakker et al. 2008; Dekel & Birnboim 2006; Brooks et al. 2009), the mechanisms whereby this material might be accreted back into galaxies remain unclear. As emphasized by Kereš et al. (2005), the multiphase nature of galactic halos plays an important role during the accretion process by modifying gas stripping and infall processes (for additional perspectives on these issues see Silk et al. 1987; Gallagher & Smith 2005; Tüllmann et al. 2006). Being close by, the MS offers a unique laboratory to study the rate and nature of gas injected from satellites, as well as models to assess the fate of the stripped gas.

The MS trails across much of the southern Galactic sky behind the Magellanic Clouds (MCs), passing near

the Southern Galactic Pole at about 1/3 of its length. It has been shown to have a continuous coherent velocity tracing across the southern Galactic sky for  $140^\circ$  (Nidever et al. 2010), just penetrating the Galactic plane at some unknown distance from the Galactic center. Direct distance constraints for the MS are difficult to establish much beyond the MCs themselves, which constrain the MS head nominally between 52 and 61 kpc, based on the MC distances established by Koerwer (2009) and Hilditch et al. (2005). With no embedded stars, no nearby ionizing sources or stellar absorption sight lines yet detected, the MCs remain its only direct distance constraint. A geometrical-dynamical analysis by Jin & Lynden-Bell (2008) found a Galactocentric distance that increased to 70 kpc at about  $90^\circ$  along the MS length. Stanimirović et al. (2008) found a similar constraint at this point assuming that the neutral hydrogen (HI) clump size distribution is driven by the Thermal Instability (TI).

Attempts to simulate the large-scale mechanism of formation and subsequent evolution of this extensive structure have focused mainly on tidal interactions with the Galaxy and/or ram pressure stripping of the MC gas by the Galactic Halo. These simulations had moderate success when it was believed that the MCs have had multiple

Electronic: lou@zooniverse.org

<sup>1</sup> Citizen Science Department, Adler Planetarium, 1300 South Lake Shore Drive, Chicago IL 60605, USA

<sup>2</sup> Department of Astronomy, University of Wisconsin Madison, 475 North Charter Street, Madison, WI 53706, USA

orbital cycles around the Galaxy (Moore & Davis 1994; Mastropietro et al. 2005; Connors et al. 2006). However, global simulations have been made difficult in recent years given the relatively new constraint that the MCs are apparently on their first pass through the Galactic system (Besla et al. 2007). Besla et al. (2010) developed a Smoothed Particle Hydrodynamics (SPH) global MS simulation in this first-pass scenario maintaining that neither tidal or ram pressure mechanisms are as sufficient as once thought to stripping the gas. Both Besla et al. (2010) and Nidever et al. (2008) propose other mechanisms to do the heavy lifting, unbinding the gas prior to stripping, through tidal resonances between the MCs in the former, and in the latter, a gas “blowout” from star formation in the LMC region that includes 30 Doradus.

Whatever the mechanism by which the gas was removed from the MCs, ram pressure, tidal effects, initial turbulent energy, magnetic field structure and subsequent interactions with the Galactic Halo all may have played a role in sculpting the rich filamentary and clumpy structure revealed in Figure 1. This figure shows the scale of the entire MS on an HI image produced by the Galactic All-Sky Survey (GASS, McClure-Griffiths et al. 2009) and takes it down in steps to a specific small, but interesting cloud toward the downstream end which is the subject of this paper. The fine scale structure revealed in the GASS image and in other recent HI observations such as Putman et al. (2003a) and Brüns et al. (2005) is not captured in the N-Body and SPH global models mentioned above. Even finer structure was revealed by Stanimirović et al. (2002, 2008) in high resolution mapping of the northern tip of the MS using the 305 meter dish at Arecibo. These observations revealed extended fine filamentary structure and clumps down to the 3.5' angular resolution of the telescope.

Several theoretical studies as well as numerical simulations have explored the effect of various hydrodynamic instabilities on the formation of small scale structure in warm gas such as the MS moving through a hot halo (Mori & Burkert 2001; Quilis & Moore 2001; Heitsch & Putman 2009). However, it is still not clear how effective these processes are and on what timescales they operate. For example, most instabilities appear to act on short timescales ( $\sim 100$  Myrs) and therefore require that the MS is continuously replenished with fresh material. The nature and evolution of the small scale MS structure (or stripped gas) is also not well understood. As such material may eventually constitute a substantial source for the MW's star formation in the form of infalling warm ionized gas (so called “warm drizzle”, Bland-Hawthorn et al. 2007), observational constraints on the physical processes operating on small spatial scales in the MS are highly important.

Numerous observational studies have revealed a multi-phase nature in MS gas. Kalberla & Haud (2006) and Stanimirović et al. (2008) showed that about 15% of the observed HI clouds have velocity profiles composed of warm and cool components, with a velocity FWHM of about  $25 \text{ km s}^{-1}$  and  $3\text{-}15 \text{ km s}^{-1}$ , respectively. Matthews et al. (2009) detected the first HI absorption lines against radio background sources in the direction of the MS close to the MCs indicating spin temperature of 70-80 K.  $H\alpha$  measurements of the warm ionized component in the MS exist (Weiner & Williams 1996;

Putman et al. 2003b), but with only a few discrete pointings and with the large  $\sim 1^\circ$  apertures, providing little insight into the processes on the small, arc minute scales.

While not being able to provide any spatial information, numerous UV and optical absorption studies have been crucial for constraining the abundance of the MS gas (Slavin et al. 1993; Fox et al. 2010). In addition, detections of O VI absorption from gas associated with the MS by Sembach et al. (2003) give strong support for the existence of an ionized component around the MS with  $T < 10^6$  K. It is generally interpreted that this component represents an interface between the hot Halo gas at  $T \sim 10^6$  K (Fang et al. 2006) and the cooler MS gas. Studies of lower ionization states suggest the existence of diffuse envelopes of somewhat cooler, partially ionized gas that is not visible in the current HI surveys. Specifically, Si III likely probes different phases than O VI with  $T = 10^{4-4.5}$  K (Shull et al. 2009) and has been detected along a sight-line in the northern MS with velocities associated with the MS (Collins et al. 2009). Recently, Fox et al. (2010) have performed an analysis of many low and high ion species in UV and optical absorption, including Si III, against background source NGC 7469. From this work, a picture emerges of a diffuse, multi-phase transition structure between the warm, mostly neutral envelope gas detected in HI and the hot, mostly ionized envelope gas detected in O VI.

As pointed out in Stanimirović et al. (2010), the rich multi-phase structure of the MS suggests cloud longevity and a slow mass ablation rate. The Kelvin-Helmholtz instability (KH) driven by shear flow between cool MS gas and the hot Halo is likely to be the dominant mode of cool cloud disruption and relatively rapid ablation compared to evaporation through pure thermal conduction. However, analytical and numerical treatments of cool gas in a hot flow suggest that the rapid ablation by KH can be moderated by factors affecting the turbulent mixture in the boundary layer. These include magnetic fields (Esquivel et al. 2006), re-cooling of heated gas (Begelman & Fabian 1990; Kwak et al. 2011) and even thermal conduction acting locally within the mixture (Vieser & Hensler 2007a).

The focus of this paper is to probe and characterize properties of this boundary layer between cool HI clouds in the MS and the surrounding Halo gas. This requires very deep HI observations, more sensitive than the existing HI surveys. For example, the predominantly ionized component detected by Collins et al. (2009) has the total column density of  $\sim 10^{18-19} \text{ cm}^{-2}$  and a neutral fraction of  $\sim 0.01$ . To detect the corresponding neutral gas we require HI column density sensitivity of  $\sim 10^{16-17} \text{ cm}^{-2}$ . This is at least 5 times lower than the most sensitive HI survey to date; GASS (McClure-Griffiths et al. 2009) which achieves  $3\sigma$  column density sensitivity of  $1.6 \times 10^{18} \text{ cm}^{-2}$ . We approach the required sensitivity by applying a new method of spatial averaging to characterize a cloud in the northern MS (shown in Figure 1) observed with very deep HI emission spectra obtained with the Green Bank Telescope<sup>3</sup> (GBT). Our analysis

<sup>3</sup> The Robert C. Byrd Green Bank Telescope is operated by the National Radio Astronomy Observatory, which is a facility of the US National Science Foundation operated under cooperative agreement by Associated Universities, Inc.

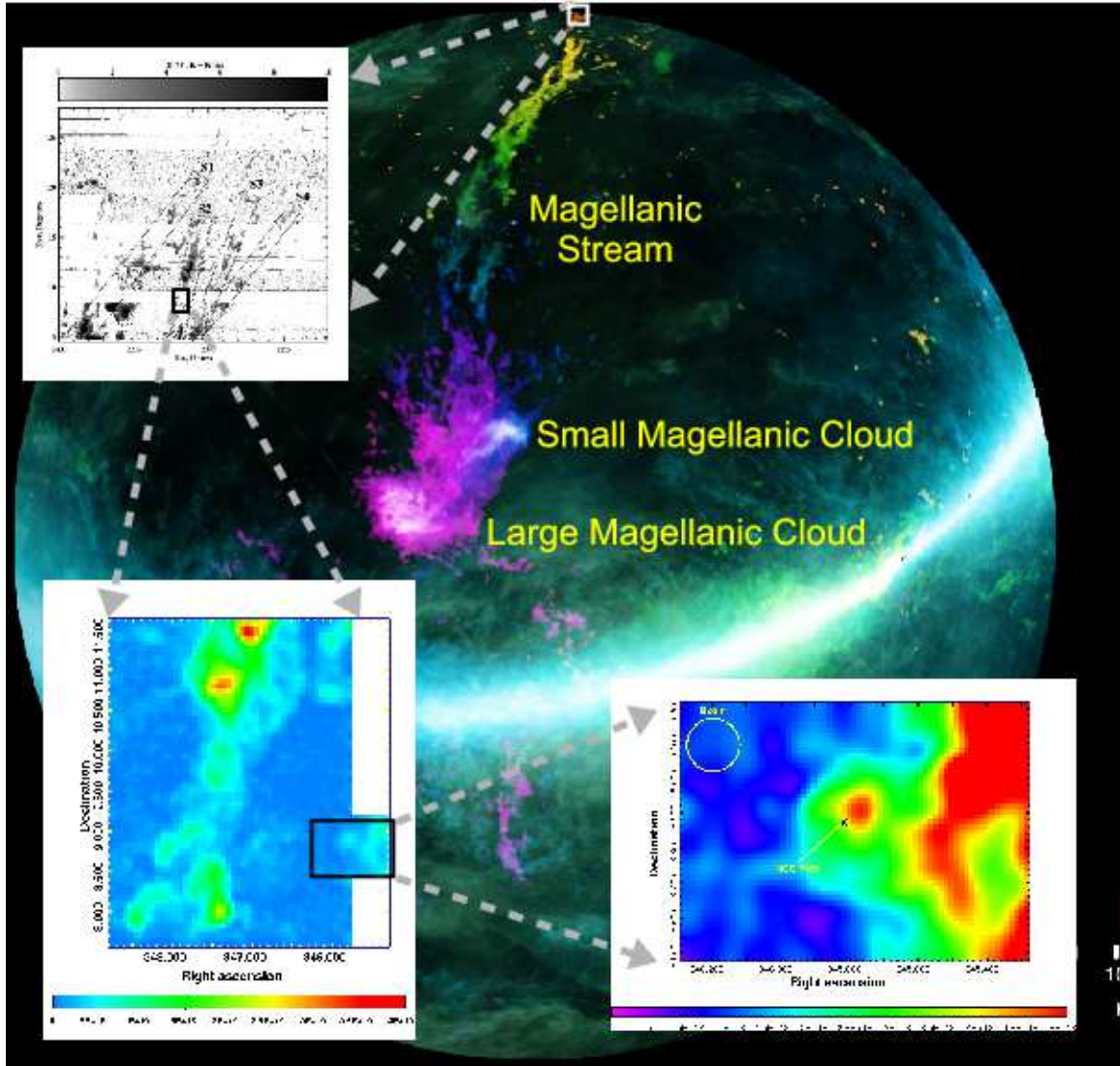


FIG. 1.— A journey in scales: From the entire MS, illustrated in the southern Galactic hemisphere map from the Galactic All Sky Survey (GASS, McClure-Griffiths et al. 2009)), down to the specific cloud studied in this paper. Counterclockwise from top: High resolution GALFA Arecibo Observatory H I map revealing fine filamentary structure in the northern MS (Stanimirović et al. 2008), high sensitivity GBT map of a section of one of those filaments (this work), and the cloud discovered in that map containing the NGC 7469 sight-line.

also benefits from the fortuitous location of the NGC 7469 Seyfert 1 background source near the cloud’s center which was extensively studied in UV and optical absorption by Fox et al. (2010) (hereafter referred to as FSW10).

Our observing and data reduction strategies are presented in Section 2. Section 3 explains the new spatial averaging method we applied to the cloud to achieve  $< 10^{17} \text{ cm}^{-2}$  sensitivity and probe the usually inaccessible cloud periphery and highly ionized cloud envelope. We also develop a simple 3D cloud model matched to our observations to obtain a robust estimate of cloud’s properties and gain insight into the internal cloud structure and processes acting at its periphery. In Sections 4.1 and 4.2, we show that the cloud properties along with results from FSW10 strongly suggest an integral WNM/WIM core transitioning to a Turbulent Mixing Layer (TML) and in Section 4.3, we investigate how consistent the cloud’s neutral density characteristics are with a photoionizing environment by comparing the model to the re-

sults of 3D ionization equilibrium simulations. Finally, in Section 4.4 we discuss the lifetime of the cloud and assess the possibility of eventually reaching the Galactic Disk where a portion of its mass could help fuel star formation. We summarize our results in Section 5.

## 2. OBSERVATIONS AND DATA REDUCTION

We used the GBT in 2009 and 2010 as part of a larger program to map several sample regions in the northern portion of the MS. One of these regions is located in the northern tip of the MS and was chosen, among other reasons, to include the NGC 7469 background source. The beam size of the GBT in the 21 cm line is  $9.1'$ , which corresponds to 183 pc at 70 kpc, a distance consistent with estimates by Jin & Lynden-Bell (2008) and Stanimirović et al. (2008) which we will assume hereafter.

Observations were obtained using the on-the-fly (OTF) mapping mode with in-band frequency switching. Constant Declination (DEC) rows were scanned and stepped

every  $3.5'$  in order to oversample the beam by 2.6 in the DEC direction. Spectra were dumped at twice that resolution so that beam-spreading in the Right Ascension (RA) direction due to scanning remained small ( $\sim 2\%$ ). The 36 second target integration time per  $3.5'$  pixel was split into four separate scans, which reduced the impact of transient signals such as Radio Frequency Interference (RFI) and spectrometer glitches. The GBT spectrometer was used with a bandwidth of 12.5 MHz and 16384 channels, corresponding to a velocity resolution of  $0.161 \text{ km s}^{-1}$ .

The GBT data were reduced using a combination of the GBTIDL and AIPS data reduction packages, and a suite of specially designed Interactive Data Language® (IDL) programs. To ensure high sensitivity, special care was taken during the baseline calibration process. First, a modified version of the GBTIDL GETFS procedure was used to obtain reference spectra to produce temperature-calibrated spectra with gross baseline calibration. Instead of using a frequency-shifted total power reference spectrum or a smoothed version of it, as is normally done, a noiseless 3rd order baseline model of a line-suppressed total power reference spectrum was used for reference. This improves the Signal-to-Noise Ratio (SNR) by  $\sqrt{2}$  without enhancing large-scale baseline structure noise which degrades its Gaussian character. The line-suppressed spectrum was obtained by selecting the minimum of either the reference or signal spectrum at each frequency. This “min filter” statistically prefers samples without a positive bias from emission of any kind and so reduces image artifacts in the final spectra and adds a fixed offset to the baseline, easily removed in the following steps. The derived reference spectrum was then used to perform a  $(\text{Signal} - \text{Reference})/\text{Reference}$  calibration of each spectrum. The spectra were then scaled by the system temperature and corrected for atmospheric opacity using the standard, built-in correction provided by GBTIDL routines.

In the next step, the calibrated and roughly baselined spectra pass through two additional baseline removal phases. Each of these include multiple steps where baselines are modeled and subtracted. In all but one case, baselines are modeled as 3rd order polynomial functions only after excluding Galactic emission and subtracting unblended Gaussian models of any detected emission lines in the spectrum. In the first phase, the baseline of the scan average for the X polarization is modeled and then subtracted from each spectrum in that scan. The baselined X emission is then subtracted from the Y polarization, effectively suppressing all emission under the reasonable assumption in this case that the emission is unpolarized. This leaves only the Y baseline, which is modeled to 7th order. This special step removes the small  $\approx 1.5 \text{ MHz}$  sinusoidal baseline component present in the Y polarization of GBT spectra, probably due to double transit reflections from the feed to the circumferential gap between main reflector panels (Fisher et al. 2003). It also removes the average offset introduced by the min filter mentioned previously. In the second step, each individual spectrum’s residual baseline differences from the average are removed in two iterations.

After baselining, spectra from identical pointings were combined and interpolated to a regular grid with pixel

size one fourth that of the sampling interval (or  $0.875'$ ) using the AIPS task SDGRD. This over-sampled the telescope beam by a factor of ten in the final data cube, providing interpolated resolution to support precise averaging along circular paths when spatial averaging techniques are applied to the cube. Velocity spectra were smoothed with a 6th order Hanning window, reducing the resolution to  $0.966 \text{ km s}^{-1}$ . The velocity range was truncated to  $-500$  to  $-200 \text{ km s}^{-1}$ . The rms noise in the final data cube was measured at  $\sigma_T = 3.4 \text{ mK}$  by averaging across emission-free velocity ranges. This corresponds to column density noise  $\sigma_N = 1.0 \times 10^{17} \text{ cm}^{-2}$  for a  $15 \text{ km s}^{-1}$  FWHM profile. This is almost four times better than the  $3.8 \times 10^{17} \text{ cm}^{-2}$  noise achieved by GASS, the most sensitive survey to date (McClure-Griffiths et al. 2009) when scaled to the same FWHM line width of  $15 \text{ km s}^{-1}$ . This sensitivity is provided at the GBT beamwidth of  $9.1'$  compared to the Parkes telescope’s  $14'$ .

### 3. RESULTS: A SIMPLE CORE + ENVELOPE CLOUD MODEL

In the data cube we unexpectedly found a roughly circularly projected, mostly isolated HI cloud in the MS, located only  $\simeq 2.5'$  from the direction of the well-studied Seyfert 1 background source NGC 7469. Figure 2 shows the HI column density (zeroth moment) and velocity (first moment, intensity-weighted) images of the cube over the velocity range  $-370$  to  $-310 \text{ km s}^{-1}$ . The cloud size is  $\approx 1.6 \times \text{beamwidth}$ . After de-convolving the telescope beam, the intrinsic cloud size is  $\approx 1.2 \times \text{beamwidth}$ . The cloud is therefore just resolved. The HI column density at the cloud center is  $\approx 5 \times 10^{18} \text{ cm}^{-2}$  and although it trails off to the north, east and south, it connects to the cloud complex to the west. The velocity image shows that this connection involves an abrupt  $\simeq -10 \text{ km s}^{-1}$  velocity shift from the  $\simeq -340 \text{ km s}^{-1}$  gas at the cloud’s apparent western edge to the neighboring  $\simeq -350 \text{ km s}^{-1}$  component labeled “A” of the western complex, which is mixed in with a nearby  $\simeq -345 \text{ km s}^{-1}$  component labeled “B”. Note also that the cloud itself has a distinct  $\simeq +5 \text{ km s}^{-1}$  gradient from west to east. The abrupt positive velocity shift from the western complex along with the continued positive gradient across the cloud suggests it may have broken off from the complex and is becoming entrained in the surrounding ambient gas.

Figure 3 shows the HI spectrum at the center of the cloud. The emission clearly has a component at  $\approx -340 \text{ km s}^{-1}$  with a FWHM  $\approx 20 \text{ km s}^{-1}$ . However, an even lower level, broad component lies at slightly more negative LOS velocities as made evident by the two-component Gaussian fit overlaid on the spectrum. The width and weakness of the wider envelope line causes us to consider the possibility that it is an artifact of the baseline removal process, but we reject that as there is independent evidence of components associated with both the core and envelope line velocities in the UV absorption spectra along the nearby NGC 7469 sight line reported in FSW10 (discussed in Section 4).

To enhance sensitivity of our observations and characterize how properties of the two components evolve outward from the cloud center, we introduce the spatial

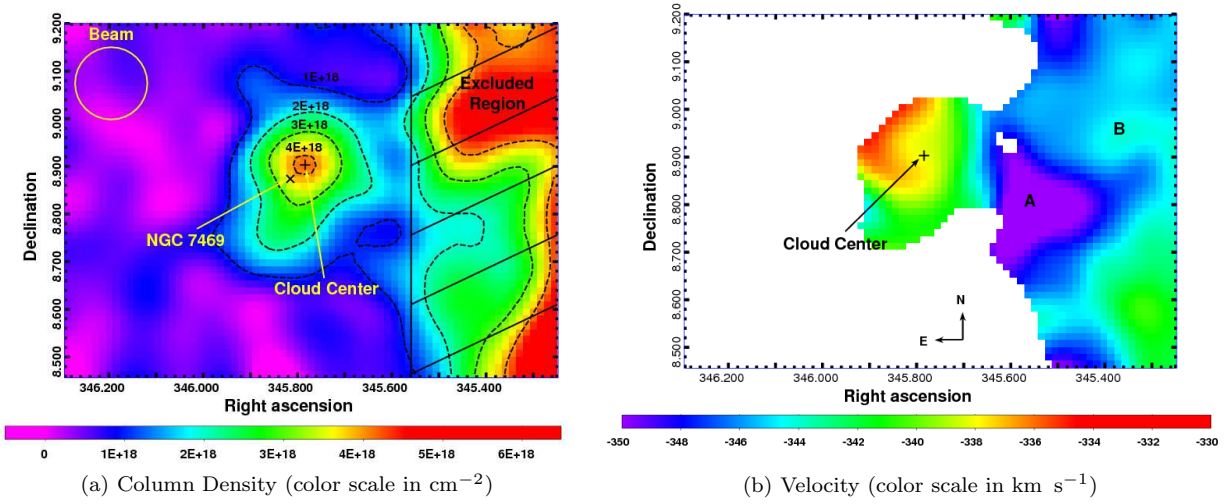


FIG. 2.— The H I column density (a) and velocity (b) images of the region containing the NGC 7469 sight line and the H I cloud that it passes through. The velocity range is  $-360$  to  $-320 \text{ km s}^{-1}$  and the velocity image column density threshold is  $2 \times 10^{18} \text{ cm}^{-2}$ . The images show that, although the large cloud complex to the west has a similar velocity range, the cloud is connected to it only by diffuse bridging gas and is well isolated in velocity. The cloud complex region was excluded from the circular path averaging as indicated.

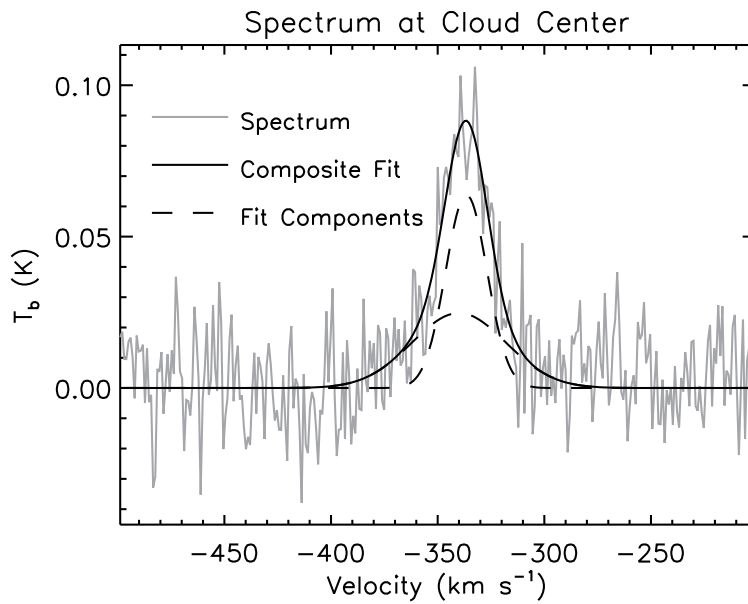


FIG. 3.— H I spectrum at the cloud center reveals two components, a  $\approx 20 \text{ km s}^{-1}$  wide component at  $\approx -340 \text{ km s}^{-1}$  on top of a weaker,  $\approx 60 \text{ km s}^{-1}$  wide component. Individual Gaussian fits to each component are shown (dashed lines) as well as the composite fit (solid line).

averaging method and apply it to the data cube in Section 3.1. This produces a profile of average column spectra versus projected angular distance,  $\rho$  from the center with increasing sensitivity, well past its apparent periphery. In Section 3.2 we purge the average profile of components that are unassociated with the cloud. Finally, in Section 3.3, we develop a simple parametric 3D spherical model of the cloud optimally matched to the purged 2D projected profile to obtain a robust estimate of the properties and structure of the cloud versus physical distance,  $r$  from its physical center outward.

### 3.1. Spatial Averaging Method: Raw cloud Profile

To perform spatial averaging of H I spectra we start with the following assumptions: (i) the cloud is roughly circularly symmetric, (ii) the cloud symmetry extends past its apparent boundaries, and (iii) along each line of sight on a circular annulus from the cloud center, H I gas has similar properties. The small velocity gradient of  $\approx +5 \text{ km s}^{-1}$  on the eastern side of the clump (Figure 2(b), discussed above) shows that the symmetry assumption is compromised, but the gradient is relatively small with respect to the width of both cloud components identified in the central spectrum of Figure 3. Its effect on the results of the averaging process that follows are considered in Sections 3.2 and 3.3.

We start from the pixel with the highest H I brightness temperature (see Figure 2) and average H I spectra spatially along circular annuli of increasing projected radius  $\rho$ . As a result, we can plot the averaged H I spectra as a function of projected angular distance from the cloud center as shown in Figure 4(a). The most important advantage of this spatial averaging method is that it reduces the noise without compromising angular resolution in the essential radial dimension, which contains most of the spatial information in the nominally circularly projected cloud. The noise improvement in the averaged spectra increases with  $\rho$  due to an increasing averaging path length, thus compensating for decreasing emission from the cloud center. Assuming infinite resolution and uncorrelated, zero mean noise at each pixel, the measurement error for a circular cloud theoretically decreases as  $1/\sqrt{2\pi\rho}$ . In reality, error improvement will be limited to the extent that the noise is zero mean and uncorrelated from pixel to pixel. The normal gridding process increases pixel-to-pixel correlation, while residual structure from imperfect baseline modeling violates both of these criteria and will generally be the limiting factor in most applications of this method. While we apply the method here to a roughly circular cloud, we note that the same method can be applied on filamentary structures by assuming linear symmetry and averaging along lines parallel to the filament main axis.

The result of the spatial averaging method is shown in Figure 4(a). On the x-axis we plot the averaged H I spectra at a given projected distance  $\rho$  from the cloud center, shown on the y-axis. The first spectrum at  $\rho = 0'$  corresponds to the single H I spectrum through the cloud center (shown in Figure 3), and is dominated by the main emission component centered at  $v \simeq -340 \text{ km s}^{-1}$ . As  $\rho$  increases, the primary emission component weakens and the broader, underlying component strengthens as the sensitivity improves. There is also a distinct blue-ward velocity gradient in the broad component spectrum as  $\rho$  increases. The distinct narrow and broad emission components of the cloud are suggestive of a spherical structure with a (kinematically) warm core and a warmer envelope: with increasing  $\rho$ , the line of sight passes through less of the core and more of the envelope and eventually, the envelope dominates through limb brightening. We explore this further through modeling in Section 3.3.

In addition to emission at the main component velocities, there appear to be one or more weak lines in the spectrum that are well separated from the main emission (*e.g.*, at  $-250 \text{ km s}^{-1}$ ) and therefore assumed to be unassociated with it. The evolving profile also contains components at similar velocities, but unrelated to the cloud’s central components as the widening circle of averaging passes through clumps of emission that are spatially separated on the sky. These are also assumed to be unassociated. In the next step, these unassociated components are purged from the projected profile.

### 3.2. Spatial Averaging Method: Profile Line Modeling

Using a semi-manual process aided by a graphically interactive program written in IDL, all H I spectra in the averaged profile were modeled as multiple, blended Gaussian functions. The process is as follows: Each H I spectrum of the profile is viewed in order of increasing

$\rho$  and initial estimates of all potential Gaussian components are provided by the user to a blended Gaussian fitting routine. Each component of the resulting fit is then checked and any with  $\text{SNR} < 2$  are removed with the remaining components used as initial conditions for a second fit. At this point, since Gaussian decomposition is not unique, the user views the fit and can accept it or try again with new initial estimates.

The result of this modeling process is shown in Figure 4(b). While many unrelated lines pop in and out with increasing  $\rho$ , there are two main Gaussian components that maintain continuity from  $\rho = 0'$  outward and so are considered to be the components of the cloud. All others are to be subtracted. It is important to stress that the purpose of this line modeling step is *not* to accurately model all the emission in the profile but only to identify and subtract components in the observed profile that are likely to be unrelated to the cloud. The resultant “cleaned” profile, which contains only the two observed primary components directly associated with the cloud, is shown in 4(c). Note that there is a prominent discontinuity in the cleaned profile which occurs at the point where the broad component becomes undetectable as part of the blended fit underneath two rising, but unrelated components that dominate it. This is an artifact of imperfect line modeling. Where the broad component is too weak to contribute its own line model to the blended fit, the other components incorporate it into their line models and then it gets subtracted.

Another limitation of the line modeling is cross-coupling, where a stronger component affects the parameters of a weaker overlapping component. These effects are not easily quantified and could dominate any uncertainties due to noise alone. Imperfections notwithstanding, the lines associated with the two components of the cloud are modeled as part of the cleaning process and provide a rough model of the cleaned profile as shown in Figure 4(d). Figure 5 shows how the modeled line width, central velocity, and H I column density parameters of these two components evolve with  $\rho$ . Figure 5(a) shows that the two components have distinctly different line widths. The narrow core component has a relatively constant FWHM  $\simeq 20 \text{ km s}^{-1}$  while the broader envelope has an apparently large outward gradient from  $\simeq 50 \text{ km s}^{-1}$  at cloud center to  $\simeq 80 \text{ km s}^{-1}$  at  $\rho \sim 20'$  where the line falls below threshold. Although the gradient may be exaggerated by parameter cross-coupling with the core component at low  $\rho$  and with subtracted components at higher  $\rho$ , it could be significant and is physically consistent with turbulent and/or thermal broadening as it approaches the hot ambient Halo medium.

The central velocity profiles of Figure 5(b) illustrate the parameter coupling concerns mentioned previously. At small  $\rho$  the stronger core component may “pull” the velocity of the weaker envelope, while the roles are reversed at  $\rho \sim 9'$ , where the core weakens and its velocity drops sharply toward the envelope’s. The sharp drop in core velocity and the step change in envelope velocity are probably not entirely real. The core velocity is likely constant for the most part at  $\simeq -336 \text{ km s}^{-1}$  with the sharp drop clearly a modeling artifact since this is not possible given the beam smoothing. The envelope’s apparent neg-

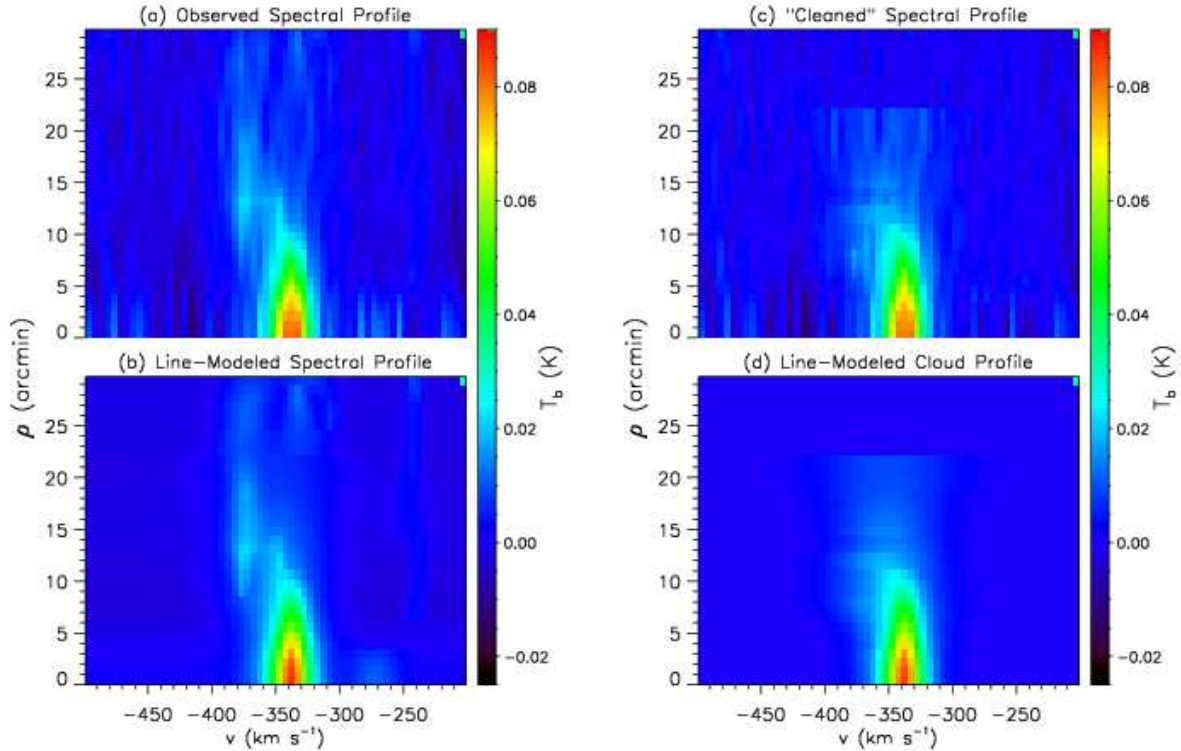


FIG. 4.— Spatially averaged spectral profiles in the line modeling phase of the analysis where the measured profile is “cleaned” of emission not related to the cloud: (a) Observed spectral profile of the cloud showing the intensity spectrum (horizontal axis) averaged along circular paths of increasing distance from the center (vertical axis). (b) Blended Gaussian emission line model of the entire profile. (c) Cleaned spectral profile of the cloud where Gaussian emission line models of all except the lines associated with the two components of the cloud’s central region are subtracted is used to constrain the optimally matched 3D parametric cloud model in the next step. (d) Lines associated with the two cloud components. For image display purposes only, profiles have been smoothed from  $0.966 \text{ km s}^{-1}$  to  $4.83 \text{ km s}^{-1}$ . Note that the vertical striations in the noise are the consequence of a noise correlation length of roughly four pixels due to interpolation.

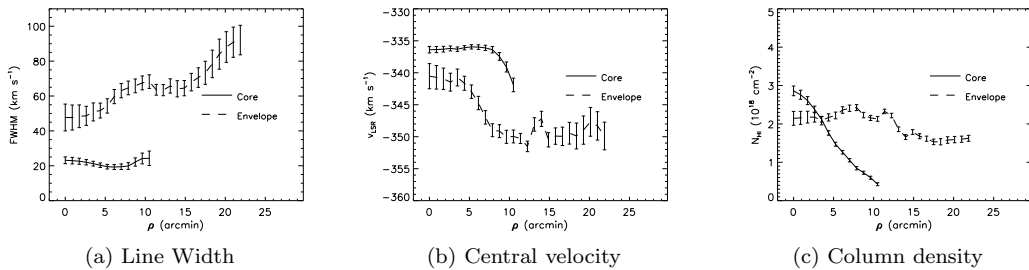


FIG. 5.— Cloud core and envelope Gaussian component line model parameter profiles. (a) Line Width (FWHM); (b) Velocity; and (c) Column Density. Error bars reflect parameter errors due to noise only. Other effects such as cross-coupling between components (see text) are not accounted for.

ative velocity gradient may be exaggerated by “pulling” from the core at low  $\rho$  but is large enough that it could be at least partially real, approaching  $\simeq -350 \text{ km s}^{-1}$  at the periphery.

Gradient or not, there *is* a difference in the central velocity between the two components of between 4 and  $14 \text{ km s}^{-1}$  with the core component clearly *lagging* the envelope component along the LOS. This is very interesting because the large negative velocity of this cloud indicates infall and a cometary morphology with the core *leading* the envelope is expected. Although the morphology may be hidden in projection or in the noise of Figure 2, the core in the spatially integrated profile is clearly lagging in velocity. This is also apparent in Figure 3

(the central cloud spectrum) indicating that this is not an artifact of the spatial averaging process. Brüns et al. (2001) similarly modeled the line profiles of HVC125+41-207 along simple perpendicular cross sections (*i.e.*, no spatial averaging) and demonstrated that its projected on-sky head-tail morphology had a cold core leading a warmer envelope. Similarly, many other HVCs with a head-tail structure have a lagging tail, which is usually interpreted as belonging to gas stripped and slowed down through interactions with the surrounding medium. This interesting, apparently anomalous velocity structure of our cloud is addressed in Section 4. Some of the gradient in line width and central velocity of Figure 5(a) and (b) could be caused by the velocity gradient asymmetry toward the eastern side of the clump. We discuss this in

### Section 3.3.

Figure 5(c) shows the well-behaved HI column density of the two components. The core component is roughly Gaussian with FWHM  $\simeq 10'$ , only slightly larger than the  $9.1'$  beamwidth. This reflects the barely resolved core. The envelope component has an almost constant column density of  $\simeq 2 \times 10^{18} \text{ cm}^{-2}$ . It is worth emphasizing that the broad envelope component which has a significant HI column density even at large  $\rho$ , constitutes a large portion of the cloud's total neutral mass and probably an even larger portion of its total mass since it is likely more highly ionized than the core. In Section 3.3 we quantify this in the context of the 3D cloud model developed there.

As a by-product of the component fitting process the residual noise of each averaged HI spectrum is measured after subtracting the line fit. This is plotted in Figure 6 as a function of projected angular distance  $\rho$  from the cloud center. This figure clearly demonstrates the extremely high sensitivity of this spatial averaging method, where  $\sigma_N$  reaches below  $4 \times 10^{16} \text{ cm}^{-2}$  at about  $10'$  from the cloud center. Also plotted is the theoretical noise as discussed in Section 3.2, which also incorporates the noise correlation effects of interpolation. Measured noise does not improve as rapidly as it could, probably because of limited resolution and residual baseline artifacts at low  $\rho$  and the correlation introduced by the gridding process as mentioned before. Note that at the beamwidth,  $\rho \approx 9'$ , correlation effects are minimal and the noise improvement approaches the theoretical limit. However, at  $\rho > 12'$ , the averaging path begins to be truncated by the excluded region and then by the borders of the cube and so the noise flattens and begins to increase.

#### 3.3. 3D Cloud Model Fitting

We now use the two-dimensional projected profile of Figure 4(c) to investigate a simple three-dimensional, core-envelope cloud model supporting our observational claims regarding the cloud structure. Since the cloud is not spatially resolved well in our measurements, subtle spatial structure in the model is not appropriate, but since spectral resolution is very high, subtle spectral structure can be incorporated. We define a spherically symmetric cloud model with three spatial and one velocity dimension as:

$$n_{HI}(r, v) = \begin{cases} \frac{n_{c0}}{\sqrt{2\pi}\sigma_c(r)} e^{-\frac{(v-v_{c0})^2}{2\sigma_c^2(r)}} & , r < r_c \\ \frac{n_{e0}}{\sqrt{2\pi}\sigma_e(r)} e^{-\frac{(v-v_e(r))^2}{2\sigma_e^2(r)}} & , r_c \leq r \leq r_c + r_e \\ 0 & , r > r_c + r_e \end{cases} \quad (1)$$

where

$$\sigma_c(r) = \sigma_{vc0} + m_{\sigma c}r, \quad (2)$$

$$\sigma_e(r) = \sigma_{ve0} + m_{\sigma e}r, \quad (3)$$

$$v_e(r) = v_{e0} + m_{ve}r, \quad (4)$$

$$r = \sqrt{x^2 + y^2 + z^2} \quad (5)$$

and cloud spatial coordinates  $x, y, z$  are defined so that the  $z$ -axis is along the LOS,  $x$  is east to west on the sky,

while  $y$  is north to south. The cloud consists of a core with a constant HI volume density  $n_{c0}$  and has a radius  $r_c$ . Beyond the core is the cloud envelope with a constant density  $n_{e0}$  which extends up to a radius of  $r_e$ . At the cloud center,  $r = 0$ , the core and envelope have a LOS velocity  $v_{c0}$  and  $v_{e0}$ , respectively. The spectra of the core and envelope are Gaussian functions centered at  $v_{c0}$  and  $v_{e0}$ , respectively. The velocity dispersion  $\sigma_v$  of the core is allowed to linearly vary with  $r$ , but the central velocity is held constant since the observed column profile (Figure 5) shows little variation. Significant gradient in the velocity and dispersion of the envelope is suggested by the profile, so both are allowed to vary linearly with  $r$ .

Note that this model incorporates a radially dependent velocity scalar field that is restricted to the LOS component of the vector field. As such, the model, although very sensitive to the directly measured LOS motions associated with a cometary feature seen in projection, is insensitive to radial motion from the cloud's 3D center. So, expansion or contraction effects cannot be inferred from the model. Parametric variables used in this model are defined in Table 1.

In practice, the function of Equation (1) was used to generate a model grid with three spatial dimensions plus one for LOS velocity. The spatial grid pixel spacing was the same as that of the observed radial profile. The grid encompassed the entire spherical cloud which spans twice the profile's radial extent in each dimension, but was extended in the  $x$  and  $y$  dimensions by two beamwidths at zero density to allow for beam smoothing. The spatial averaging method was applied to the 3D model by summing the spectra in the  $z$  direction at each  $(x, y)$  pixel to obtain a spectral profile to be compared with the observed cloud profile. The weighting used was the inverse of the measured profile variance at each pixel. Prior to comparing simulated and observed profiles, the model array was processed to simulate observing effects. This involved approximate beam smoothing with a 2D Gaussian having FWHM equal to the GBT beamwidth, truncated at  $\pm$ FWHM. An equivalent averaging of spectra along circular paths was then applied as was done in the case of the observed data cube.

We used the AMOEBA algorithm (Nelder & Mead 1965) to find the model parameters that minimize the weighted least mean-squared error of the 3D model's simulated observed profile. AMOEBA finds the local minimum in the parameter space that is nearest to the initial guess. All of the parameters in this model relating to the velocity spectrum shape are easily estimated from and well constrained by the observed profile data. They are also relatively independent of the core and envelope sizes. For these parameters, the error surface should be well behaved with a single minimum. The core and envelope sizes and densities are highly inter dependent, and the error surface would have a very broad minimum given that the beam smoothing is comparable to the profile's scale width. Also, there may very well be multiple minima. Because of these concerns, a sweep of the initial guesses for these two size parameters was performed in order to find the lowest local optimum over a range of values. For each combination of initial core and envelope size guesses, approximately self-consistent initial density values were derived from the observed column density at  $\rho = 0$  and  $\rho \approx r_c$ , respectively. The optimization

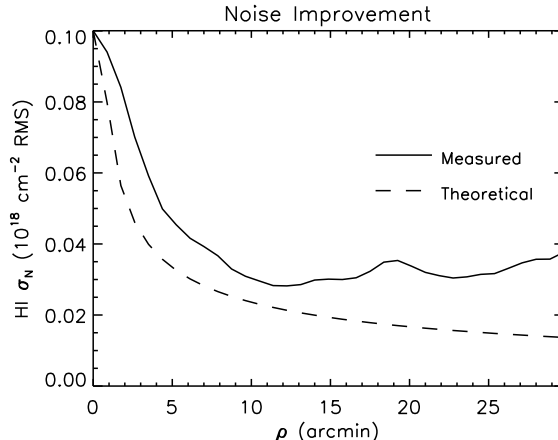


FIG. 6.— The measured RMS noise of the HI column density for a  $15 \text{ km s}^{-1}$  FWHM line (solid line) versus the projected distance from the cloud center. Also shown is the theoretical error improvement (dashed line) assuming zero mean, uncorrelated noise and infinite resolution. Measured noise does not improve as quickly at first partially because the effects of finite resolution are more important for short averaging paths. Note that close to  $\rho \sim 11'$  measured noise approaches the theoretical value of  $2.4 \times 10^{16} \text{ cm}^{-2}$ , and then increases due to path truncation from exclusion of the western region of the cube. This is a very deep measurement and maintains error in the periphery below  $4.0 \times 10^{16} \text{ cm}^{-2}$ .

TABLE 1  
CORE PLUS ENVELOPE MODEL OPTIMIZED PARAMETERS

Parameter	Description <sup>a</sup>	Value
$r_c$	Core normalized radius (arcmin)	$7.32 \pm 0.37$
$n_{c0}$	Core number density at center ( $\frac{70 \text{ kpc}}{D} \text{ cm}^{-3}$ )	$(5.27 \pm 0.41) \times 10^{-3}$
$v_{c0}$	Core velocity ( $\text{km s}^{-1}$ )	$-336.3 \pm 0.2$
$\sigma_{vc0}$	Core velocity dispersion at center ( $\text{km s}^{-1}$ )	$8.80 \pm 2.94$
$m_{\sigma c}$	Core velocity dispersion slope ( $\frac{\text{km s}^{-1}}{\text{arcmin}}$ )	$0.20 \pm 0.61$
$r_e$	Envelope normalized thickness (arcmin)	$18.51 \pm 0.41$
$n_{e0}$	Envelope density ( $\frac{70 \text{ kpc}}{D} \text{ cm}^{-3}$ )	$(8.83 \pm 0.26) \times 10^{-4}$
$v_{e0}$	Envelope initial velocity ( $\text{km s}^{-1}$ )	$-349.6 \pm 0.4$
$m_{ve}$	Envelope velocity slope ( $\frac{\text{km s}^{-1}}{\text{arcmin}}$ )	$-0.441 \pm 0.264$
$\sigma_{ve0}$	Envelope initial velocity dispersion ( $\text{km s}^{-1}$ )	$25.8 \pm 3.0$
$m_{\sigma e}$	Envelope velocity dispersion slope ( $\frac{\text{km s}^{-1}}{\text{arcmin}}$ )	$0.157 \pm 0.253$

<sup>a</sup> Scalable units use  $D$ , the LOS distance in pc.

was run at these combinations and the solution with the minimum error at optimum was chosen. Optimized parameter values are shown in Table 1 along with  $1\sigma$  error estimates. The parameter error vector  $\Delta \mathbf{p} = (\Delta p_n)$  was estimated by taking the square root of the diagonal elements of the covariance matrix  $[\mathbf{J}^T \mathbf{W} \mathbf{J}]^{-1}$ . Here,  $\mathbf{W} = [1/\sigma_m^2]$  is the diagonal weighting matrix used in the optimization,  $\sigma_m$  are measured error vector elements (flattened matrix of rms noise residuals from line modeling), and  $\mathbf{J} = [J_{mn}] = [\frac{\partial y_m}{\partial p_n}]$  is the Jacobian matrix at the optimum solution (determined numerically).

Figure 7 shows the cloud modeling results. Figure 7(a) is the spatially averaged observed projected spectral profile purged of all but the main emission component (same as in Figure 4(c)), used as the optimization target for the AMOEBA algorithm. Figure 7(b) is the projected spectral profile of the optimized 3D cloud model without beam smoothing effects, Figure 7(c) is the same as (b) with beam smoothing, which is used to compare with *i.e.*, subtract from, (a) in the optimization process. Figure 7(d) shows the residual from this subtraction. The residual structure at  $\rho$  from  $\simeq 20$  to  $24'$  is a consequence

of the optimization “smoothing” out the discontinuity in the cleaned envelope emission at the points where it meets line detection threshold. The low residual levels in the image show that our simple core-envelope 3D cloud model, when similarly projected onto a 2D spectral profile, clearly compares well with the observed data. This supports our interpretation of narrow and broad velocity components tracing internal structure of a single HI cloud.

The quality of the fit for the model is quantified by comparing the RMS of this modeling residual,  $\sigma_{model} = 6.17 \text{ mK}$  (calculated between  $-450$  and  $-250 \text{ km s}^{-1}$ , the range of emission), to the RMS noise of the observed profile,  $\sigma_{noise} = 6.20 \text{ mK}$  measured in the previous line modeling step. This represents a  $\sqrt{|\sigma_{model}^2 - \sigma_{noise}^2|} = 0.7 \text{ mK}$  RMS modeling error, only 11% of the noise. The simplicity of this model and the low residual error strongly suggest that this is a reasonable representation of the observed data. We therefore proceed with further data analysis under the core-envelope cloud model.

The model parameters are summarized in Figure 8, where values of HI volume density, central line veloc-

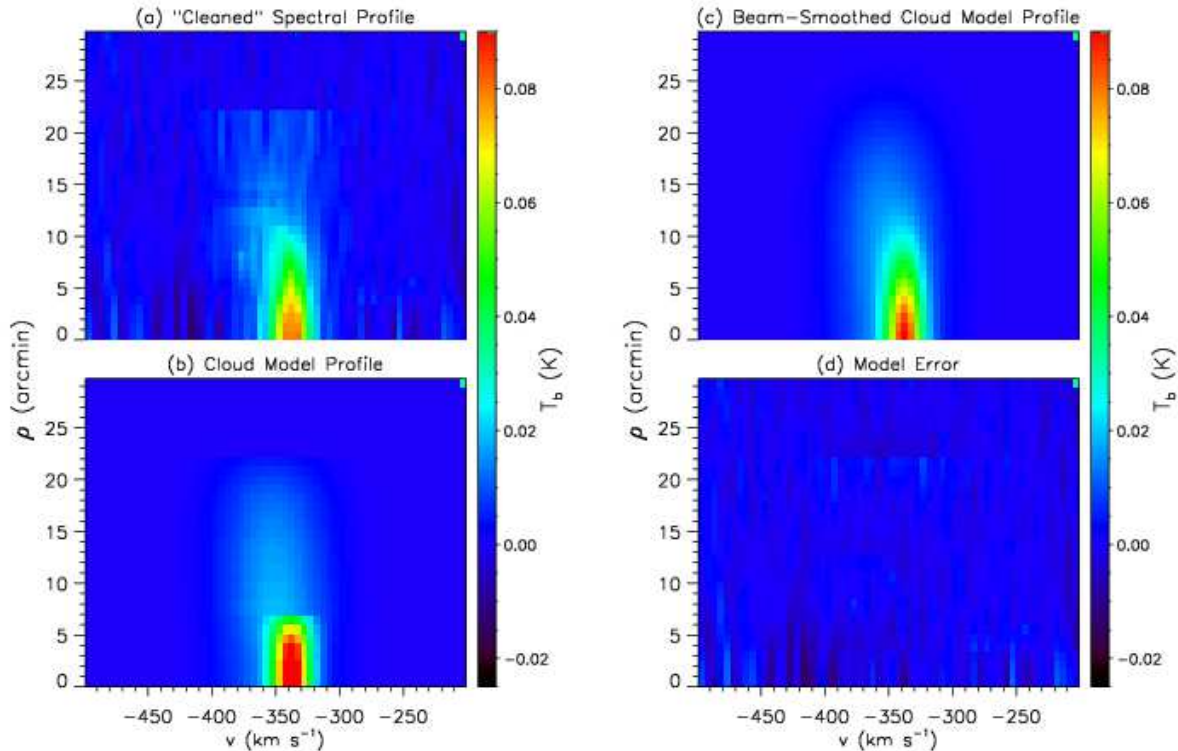


FIG. 7.— Cloud modeling results: (a) Cleaned spatially averaged spectral profile purged of non-cloud components. (b) The projected spectral profile of the two-component 3D cloud model without beam smoothing. (c) The projected model profile with beam smoothing. (d) The model profile residual error, or the difference between the cleaned profile and the beam-smoothed model profile. For image display purposes only, profiles have been smoothed from  $0.966 \text{ km s}^{-1}$  to  $4.83 \text{ km s}^{-1}$ .

ity and line width for the two components are plotted as a function of radial distance,  $r$  from the cloud center. The best-fit values for the HI volume density of the cloud core and envelope are  $5.3 \times 10^{-3}$  and  $8.8 \times 10^{-4} \text{ cm}^{-3}$ , respectively, scaled to a reference distance of 70 kpc. For comparison, using an independent method Stanimirović et al. (2002) estimated the HI volume density for several MS clouds in this part of the MS at  $\sim 5 \text{ cm}^{-2}$  assuming a distance of 60 kpc. The density of the modeled core scaled to this distance translates to  $6.1 \times 10^{-3} \text{ cm}^{-3}$ , which is  $\sim 1/8$  of that estimate, but the former is based on clumps with  $> 5$  times the central column density so a higher neutral fraction is to be expected due to more effective self-shielding. The LOS velocity of the model core is constant, as constrained by the model, and the nominal velocity of the envelope gradually decreases from  $-344$  to  $-351 \text{ km s}^{-1}$ . The error bars indicate considerable uncertainty in this gradient which is only  $\simeq 10\%$  of the line width.

As mentioned previously, the small observed asymmetry in the observed velocity field in Figure 2(b) could contribute to the velocity centroid and width gradients observed in Figure 5 (and modeled in Figure 8). We can estimate the magnitude of this effect by quantifying the observed velocity gradient asymmetry in the core, assume that it continues into the envelope, and then estimate its affect on the model's averaged gradients. From Figure 2(b),  $\simeq +5 \text{ km s}^{-1}$  gradient occurs over approximately one beamwidth, or  $\approx 10'$  resulting in a velocity gradient of  $\approx +0.5 \text{ km s}^{-1} \text{ arcmin}^{-1}$ . Since the asymmetry is present for less than one-half of the averaging

path, the combined effect is about one-half the measured gradient, or  $\approx +0.25 \text{ km s}^{-1} \text{ arcmin}^{-1}$ . Referring to Table 1, note that this could account for most of the observed core line width gradient  $m_{\sigma_c}$  which is dominated by the uncertainty due to noise anyway, so the effect of the asymmetry on the core line width gradient is insignificant. The model did not include a core velocity gradient because there appeared to be little variation, but this positive gradient asymmetry may have compensated for a roughly equal and opposite gradient amounting to only  $\approx 2 \text{ km s}^{-1}$  across the  $\approx 7'$  radius of the core. We also note that the negative envelope line width gradient  $m_{\sigma_e}$  could be partially compensated by the asymmetry, but the  $\approx +0.25 \text{ km s}^{-1} \text{ arcmin}^{-1}$  effect is comparable to the error due to noise and so not of significant concern.

Table 2 summarizes the global properties of the model cloud in more physically relevant terms useful for discussion in Section 4. Those properties that are distance-dependent are scaled for a reference distance of 70 kpc LOS. The units indicate how the quantities scale at other distances. It is particularly noteworthy that while the envelope has about a factor of two lower HI column density, it is quite extended and is seven times more massive than the core.

#### 4. PHYSICAL INTERPRETATION OF THE MODEL

Using the highly sensitive analytical technique based on a simple 3D parametric model described in Section 3, we have obtained observational evidence of the cloud having a distinct neutral core with a WNM-like velocity line width, surrounded by an envelope with a much wider line width, described by the model parameters of

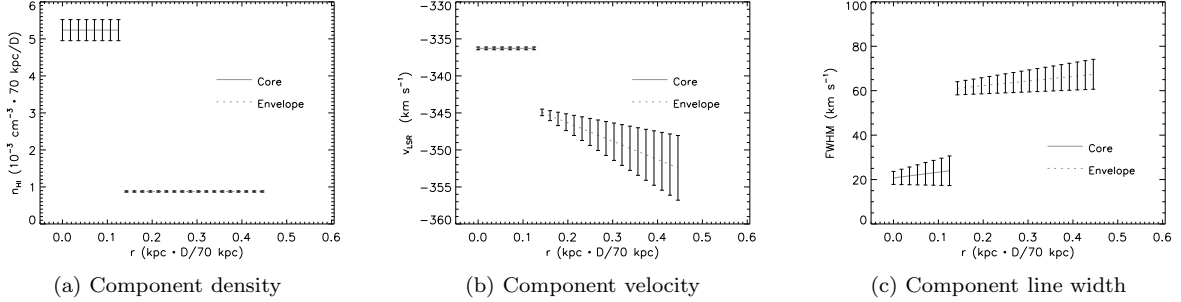


FIG. 8.— Characteristics of the optimized two-component core-plus-envelope spherically symmetric cloud model: (a) Stepped uniform density profile as imposed by the model. (b) The velocity profile shows an abrupt blue-ward shift at the core-envelope transition followed by a moderate blue-ward gradient in the envelope, suggesting an outward motion of the core with respect to the envelope, but both are only  $\sim 15\%$  of the envelope line width and therefore, not very significant. (c) Line width profile with the core consistent with a WNM phase, and the envelope  $\sim 9\times$  kinematically warmer. The line width gradients are not significant given the errors, but consistent with warming and/or increasing turbulence toward the periphery. These small velocity and line width gradients may also include the effects of a small asymmetry in the velocity structure of the cloud (see text).

TABLE 2  
MODEL CLOUD PROPERTIES

Parameter	Description <sup>a</sup>	Value
$[l, b]$	Galactic coordinates (deg)	$[83, -45]$
$\theta_{lg}$	LOS to Galactocentric angle, $D > 50$ kpc (deg)	$< 9.4$
$r_c$	Core radius ( $\frac{70}{D}$ pc)	147
$\bar{n}_c$	Mean Core neutral density ( $\frac{70 \text{ kpc}}{D} \text{ cm}^{-3}$ )	$5.3 \times 10^{-3}$
$\bar{\sigma}_{vc}$	Mean Core velocity dispersion ( $\text{km s}^{-1}$ )	10
$\bar{v}_c$	Mean Core LOS velocity ( $\text{km s}^{-1}$ )	-336
$N_{HIc}$	Central Core H I column density ( $\text{cm}^{-2}$ )	$4.8 \times 10^{18}$
$M_{HIc}$	Core H I mass ( $(\frac{D}{70 \text{ kpc}})^2 M_\odot$ )	$2.5 \times 10^3$
$r_e$	Envelope thickness ( $\frac{D}{70 \text{ kpc}}$ pc)	380
$\bar{n}_e$	Mean Envelope neutral density ( $\frac{70 \text{ kpc}}{D} \text{ cm}^{-3}$ )	$8.9 \times 10^{-4}$
$\bar{\sigma}_{ve}$	Mean Envelope velocity dispersion ( $\text{km s}^{-1}$ )	29
$\bar{v}_e$	Mean Envelope LOS velocity ( $\text{km s}^{-1}$ )	-358
$N_{HIE}$	Central Envelope H I column density ( $\text{cm}^{-2}$ )	$2.1 \times 10^{18}$
$M_{HIE}$	Envelope H I mass ( $(\frac{D}{70 \text{ kpc}})^2 M_\odot$ )	$1.8 \times 10^4$
$M_{HI}$	Total H I mass ( $(\frac{D}{70 \text{ kpc}})^2 M_\odot$ )	$2.1 \times 10^4$
$M_{Hmin}$	Minimum total H mass <sup>b</sup> ( $(\frac{D}{70 \text{ kpc}})^2 M_\odot$ )	$4.1 \times 10^5$

<sup>a</sup> Scalable units use  $D$ , the LOS distance in pc.

<sup>b</sup> Assumes  $\text{H II}/\text{H I} > 19$  (Fox et al. 2010)

Figure 8. We now delve into physical interpretations of the observed spatial and kinematic structure.

The most interesting and puzzling aspect of our results so far is the negative velocity offset of the envelope with respect to the core which ranges from  $-5 \text{ km s}^{-1}$  at the center and gets larger further out to  $-10 \text{ km s}^{-1}$  implying that in this infalling structure, the envelope, presumably consisting of gas components stripped from the core and entrained by the relatively static Halo, is falling faster, *leading* the core. We would expect a typical cometary feature to develop with entrained, envelope gas trailing behind the core with a *lagging* velocity as found by Brüns et al. (2001) in a structural analysis of HVC125+41-207 previously mentioned in Section 3.2. Their analysis of highly resolved observations of the HVC revealed WNM-like gas in a cometary envelope surrounding a well-resolved CNM-like core. In contrast, our cloud’s barely resolved WNM core corresponds to their entire cloud and our envelope corresponds to possible boundary gas surrounding their HVC, well be-

low their detection threshold. Still, we might expect an analogous structure in the boundary gas, in transition to the Halo. Our cloud shows no clear projected on-sky cometary feature, but given the high LOS velocity it would probably be hidden in full projection behind the cloud. However, this orientation would directly show the lagging envelope velocity signature of a cometary feature yet we see it clearly leading.

The most likely explanation for the leading envelope is suggested by the velocity structure of Figure 2(b) which, as discussed in Section 3, indicates the cloud may be a large clump of entrained gas originating from the western complex and now lagging it. The detected envelope velocity range of  $\simeq -350 \text{ km s}^{-1}$  to  $\simeq -345 \text{ km s}^{-1}$  corresponds closely to the velocity range of the two nearby components (A and B) of the western complex. The detected envelope therefore, may be an extended, diffuse structure that both the cloud and the western complex are embedded in. Although of low H I column density,  $\sim 2 \times 10^{18} \text{ cm}^{-2}$ , it is quite extensive and may contain

a significant amount of HI.

However, our spatial averaging method provides further constraints on the nature of the diffuse envelope. Since the region excluded in the spatial averaging includes most of the extended structure and bridging gas to the west past  $\simeq 14'$  from the cloud center, our 3D cloud model is not influenced by this western region. We can therefore assume that although the projected circular symmetry assumption of the averaging method is weaker, the core-envelope cloud model (Section 3.3) reasonably represents properties of the envelope gas in the vicinity of the cloud, suggesting a physical association between the cloud core and its immediate envelope. Therefore, we proceed with interpretation under the assumption that the core is embedded in the surrounding envelope, but that the envelope is part of a larger structure in the local hierarchy closely associated with the core.

In addition to our HI observations, the UV spectroscopy of NGC 7469 by FSW10 provides rich complementary information about the cloud. Numerous absorption lines have been detected from both low and high ionization species at MS velocities. FSW10 concluded that neither photoionization nor single-temperature collisional ionization can explain the observed column densities of high ions. This suggested the existence of highly multi-phase plasma, with a cooler region traced by SiIV (peaking at  $10^{4.8}$  K), and a hotter region being traced by OVI (peaking at  $10^{5.5}$  K). On the other hand, the detected low ionization species of OI, CII and SiII trace WNM and WIM gas with a temperature  $< 10^4$  K as does HI.

Table 3 summarizes the parameters of our observation-based HI model components (calculated along the same sight line) and measured components of three of the low ions from FSW10. The core component central velocities line up quite well within a few  $\text{km s}^{-1}$  of the HI and the wider component central velocities are also quite close, but have a wider range. The velocity dispersions,  $\sigma_v$  of the core components are all comparable, but those of the envelope velocity are widely scattered. We interpret these data in the following sections.

#### 4.1. Cloud Envelope

##### 4.1.1. Smooth conduction-dominated boundary layer

The detected envelope HI line has an average modeled velocity dispersion  $\sigma_{ve} = 29 \text{ km s}^{-1}$  (Table 2) which does not vary significantly across its full extent, which is  $2.6 r_c$  (Figure 8). Although the observed velocity FWHM might suggest a slight increase away from the cloud center, this is not well constrained with our angular resolution. This dispersion is  $\sim 3$  times higher than what is expected for the WNM/WIM gas at  $\sim 10^4$  K and could be interpreted as being due to gas at kinetic temperature  $T < 1.0 \times 10^5$  K with an additional turbulent component. One possible explanation is that the envelope represents a conduction-dominated (evaporative) boundary layer, along the lines of Cowie & McKee (1977), in relatively smooth transition from the  $\sim 10^4$  K WNM/WIM core to the  $\sim 10^6$  K WIM Halo. We do not consider radiative effects on the interface as analyzed by McKee & Cowie (1977) since the estimated core radius of 147 pc (Table 2) is well below the critical radiation radius,  $R_{rad}$  defined in that analysis as the radius above which radi-

ation effects become significant. The analysis, based on cooling at solar metallicity yields  $R_{rad} > 1.6 \text{ kpc}$  for an assumed final (Halo) temperature  $T > 10^6$  K and density  $n < 10^{-4} \text{ cm}^{-2}$  (Sembach et al. 2003). This is already much larger than our estimated cloud radius. The lower metallicity in this part of the MS of  $\sim 0.1$  solar (Fox et al. 2010) implies a lower cooling rate. Thus the mean free path in the boundary layer, represented by the scale length  $\lambda(T)$ , increases (McKee & Cowie 1977, Equation 7) making for an even higher critical radius. This makes the non-radiative assumption even more comfortable.

Interpreting the envelope as single-phase gas in a conduction-dominated boundary layer, we first estimate the maximum detectable gas temperature that would leave sufficient neutral fraction to produce the observed  $2.1 \times 10^{18} \text{ cm}^{-2}$  neutral envelope column density (Table 2) through a realistic column depth. A rough equilibrium calculation was performed for Hydrogen using an approximate collisional ionization formula (Draine 2011, Equation 13.11) and interpolated recombination rate coefficients (Spitzer 1998, Table 5.2) under optically thin conditions. It showed that envelope gas of density  $< 0.011 \text{ cm}^{-3}$  (twice the core neutral density of Table 2) at a temperature  $> 3.8 \times 10^4$  K, would be so highly ionized as to require a column  $> 140 \text{ kpc}$  (twice the assumed distance) to obtain the measured column density. So, the observed envelope would have to trace gas no warmer than  $3.8 \times 10^4$  K, with kinetic (thermal) dispersion  $\sigma_k < 18 \text{ km s}^{-1}$ . Given the kinetic component, the turbulent component required to produce the total dispersion would have  $\sigma_t > 23 \text{ km s}^{-1}$ .

Although no conduction-dominated analyses or simulations that we are aware of consider intrinsically turbulent cloud structure, they predict the temperature profiles of static (evaporative/condensing) boundary layers. Dalton & Balbus (1993) considered both classical and saturated heat flux and derived temperature profiles as a function of  $r/r_c$  and the global saturation parameter,  $\sigma_0$ . In Gnat et al. (2010) Figure 1, these profiles are plotted for a range of  $\sigma_0$  values. In our case, we assume  $T_{HIM} = T_{Halo} > 10^6$  K and for our estimated maximum envelope temperature, we have  $T/T_{HIM} < 3.8 \times 10^4/10^6 = 0.038$  where  $r/r_c$  gets only slightly larger than one, regardless of saturation parameter. This would make the transition to our maximum envelope temperature on order of  $0.01 r_c$ . In fact, even if the above detectability analysis is ignored and assuming the envelope dispersion is completely thermal, with corresponding  $T_{max} = 1.0 \times 10^5$  K, the transition distance is still only on order of  $0.1 r_c$ . This is clearly inconsistent with our extensive detected envelope which reaches a distance of  $2.6 r_c$  beyond the core.

Vieser & Hensler (2007b) performed simulations that included classical and saturated heat flux (their model R3) for a cloud of similar total mass to ours and under ambient temperature and density on the same order as the Halo. Although nearly sonic flows and a thin turbulent layer ( $\sim 5\%$  of  $r_c$ ) developed in these simulations, no systemic turbulence developed nor was it considered. The initial cloud radius, at 41 pc, is less than 1/3 the size of our cloud, but we assume that things roughly scale with radius and ambient temperature as do the derived profiles of Dalton & Balbus (1993). A temperature pro-

TABLE 3  
LOW ION LINE PROPERTIES TOWARD NGC 7469

Line	$E_{i+1}^a$ (eV)	Core		Envelope	
		$v_0$ (km s <sup>-1</sup> )	$\sigma_v$ (km s <sup>-1</sup> )	$v_0$ (km s <sup>-1</sup> )	$\sigma_v$ (km s <sup>-1</sup> )
H I 21 cm <sup>b</sup>	13.6	-336 ± 0.2	9.7 ± 5.0	-357 ± 0.4	28 ± 5
O I $\lambda$ 1302.168 <sup>c</sup>	13.6	-337 ± 1	5.6 ± 1.4	-364 ± 1	4.2 ± 4.2
Si II $\lambda$ 1260.422 <sup>c</sup>	16.3	-335 ± 1	7.1 ± 1.4	-368 ± 2	9.2 ± 2.8
C II $\lambda$ 1334.532 <sup>c</sup>	24.4	-330 ± 1	9.2 ± 1.4	-360 ± 1	16.3 ± 2.8

<sup>a</sup> Ionization potential to next level.

<sup>b</sup> This work, mean model values 2.5' off-axis (toward NGC 7469) with 9.1' beam.

<sup>c</sup> FSW10 Table 1,  $b$  values scaled to  $\sigma_v$ , aperture is  $0.2 \times 0.06''$ .

file is not provided, but if we interpret the density profile of their Figure 12 assuming roughly constant pressure, the steep drop in density from  $r/r_c \approx 1$  to about 10 times that of the ambient Halo at  $r/r_c \approx 1.2$  suggests the temperature at that point would be  $T \sim 10^5$  K for  $T_{Halo} \sim 10^6$  K. From this temperature profile, our detected envelope gas should extend no further than 20% of core radius (again assuming that the velocity dispersion is purely thermal). This is much further than the Dalton & Balbus (1993) profiles predict, but still less than an order of magnitude as deep as our observed envelope, which extends as far as 260% of core radius, even after convolution with the GBT beam is taken into account. Vieser & Hensler (2007b) also simulated the cloud with self-gravity (their model R4) and then again with cooling/heating added (their model R5), with each compressing the transition range further. We can therefore state that our observed envelope extends further, *by more than an order of magnitude*, than simulated or derived results predict for an evaporating cloud without systemic turbulence. The impact that turbulence throughout our core and envelope would have on these predictions is not known, yet one would expect it to be significant. However, an order of magnitude increase in the extent of the low temperature range of the boundary layer seems unlikely.

#### 4.1.2. Turbulent mixing layer

As an alternative interpretation, the large velocity dispersion of the cloud envelope may be the result of the superposition of multiple, more or less independent clumps of WNM/WIM gas turbulently intermixed in the boundary layer with warmer phase gas along the lines of the Turbulent Mixing Layer (TML) described in Begelman & Fabian (1990). This approach provides a simpler and more supportable explanation for our observations. In this picture the broad velocity width of the envelope is due to the superposition of discrete clumps of  $\sim 10^4$  K WNM gas (as found in the cloud core, Table 2), photoionized by the background and Galactic UV radiation, and turbulently dispersed in a mixture with much warmer gas approaching HIM temperatures with  $T \sim 10^5$  K. The superposition of multiple WNM ( $\sim 10^4$  K) clumps, each with  $\sigma_{vc} \sim 10$  km s<sup>-1</sup> turbulently dispersed with  $\sigma_t \sim 27$  km s<sup>-1</sup> will produce an approximate Gaussian shape with  $\sigma_{ve} \sim 29$  km s<sup>-1</sup>, similar to the observed total envelope dispersion.

The low metal ion envelope velocity dispersions of Table 3 should also be consistent with this picture. O I and Si II envelope components have comparable dispersion, but are very low compared to H I. C II has significantly higher dispersion than O I and Si II, yet less than H I. It is important to emphasize that H I is observed with a 9.1' beam and averaged all around the cloud's vicinity through the spatial averaging we applied, so it would sample a large number of these WNM clumps over a wide range of dispersed velocities. On the other hand, the metal ions are observed with a "pencil" beam through the center of the cloud, passing through a much smaller number of the clumps and having a smaller dispersion. The larger C II dispersion could be explained by its significantly higher ionization potential allowing it to survive into warmer and more turbulent gas surrounding the WNM clumps.

The TML model, first suggested by Begelman & Fabian (1990), explains turbulent mixing of cool and hot gas arising from the KH or shear instability induced by the velocity difference across the interface between the two types of gas. The TML consists of a continuum of phases between the cooler  $\sim 10^4$  K (WNM/WIM) stripped gas and intermediate temperature gas at  $\bar{T} = \sqrt{T_{cool}T_{hot}} \sim 10^5$  K (assuming  $T_{hot} = T_{Halo} \sim 10^6$  K) coexisting in a turbulent mixture. Also, since cooling is very efficient at this intermediate temperature, they suggest that some of the ablated gas would rejoin the cooler phase rather than be lost to the hot phase gas, a possible means for slowing the ablation process and extending cloud lifetime.

Hydrodynamic simulations of WNM gas clouds passing at supersonic velocities through the HIM provide further qualitative support to our observations. In simulations, WNM clouds consistently develop a hierarchy of smaller clumps peeling off the cloud as a result of KH instability, similar to the picture of WNM/WIM clumps we propose (Esquivel et al. 2006; Vieser & Hensler 2007a; Heitsch & Putman 2009; Kwak et al. 2011). In the present case, our cloud core is probably a very large clump recently separated from the western complex of Figure 2 as discussed above. Another consistent feature of the simulations is the development of vorticular flow along the shearing interface of the main cloud as well as clumps and protuberances that develop there. A most striking example are the early evolution simulations shown in Figure 2 of Vieser & Hensler (2007a) where vor-

tices are fully developed in the non-conductive case and appear to be forming in the more slowly developing conductive case. In the longer-term multi-ion simulations of Kwak et al. (2011) the material is tracked as the developing TML entrains it. The simulation represented in their Figure 2 extend to much larger times and the cloud has properties more like our cloud than the simulations of Esquivel et al. (2006) or Vieser & Hensler (2007a). As the gas falls behind the HVC it mixes with the ambient gas producing intermediate temperature gas. The temperature and velocity structure of the ablated material increases in complexity and range with time. At later times, the simulations indicate a wide  $10^3$  to  $10^{5.5}$ K temperature range in the ablated material mixture with  $\sim 40 \text{ km s}^{-1}$  of velocity range in the  $\sim 10^4$  K gas near the cloud axis. This is similar to the observed velocity dispersion of the H I envelope. Also significant, although not easy to discern in Figure 2 of Kwak et al. (2011), is the vorticular transport of gas from the mixing layer to the central region where it reverses direction with respect to the entrained gas as discussed by the authors. They also describe it as a means by which gas cooled in the mixing layer replenishes the cooler gas at the center as suggested by Begelman & Fabian (1990) and mentioned above. This vorticular motion in the simulations is consistent with our proposed picture of clumps dispersed in both leading and lagging velocities with respect to the cloud in our observed envelope.

#### 4.2. Cloud Core

The observed H I core component, with its mean line width consistent with  $T < 1.2 \times 10^4$  K, is reasonably interpreted as the neutral component of a central concentration of moderately turbulent WNM to WIM supplying cooler gas to the TML after being stripped from its periphery. The kinetic temperature  $T$  and turbulent dispersion  $\sigma_t$  of the gas can be estimated from the line velocity dispersions,  $\sigma_1$  and  $\sigma_2$  of two co-spatial species with atomic masses  $m_1$  and  $m_2$  by solving the two equations:

$$\frac{k_b T}{m_1} + \sigma_t^2 = \sigma_1^2 \quad (6)$$

$$\frac{k_b T}{m_2} + \sigma_t^2 = \sigma_2^2. \quad (7)$$

More than one species could be incorporated by finding an optimum solution for a set of equations for all co-spatial species, of course.

The components of the three metal species at or near the H I core velocity listed in Table 3 should sample a line of sight through the WNM core and the (photoionized) WIM envelope that probably surrounds it. However, they may not all be strictly co-spatial. The density profile of each species can be quite different along the line of sight due to different ionization potentials responding to a decreasing UV flux toward the shielded core center. H I and O I have the lowest ionizing potentials and so survive mostly toward the center and concentrate there. Si II and C II have much higher potentials and, surviving the higher flux in the periphery, are distributed more evenly throughout the core. Unless gas along the line of sight has a uniform temperature and turbulent dispersion out to a distance where Si II and C II are mostly

depleted, these two ions would be biased with respect to H I by sampling gas near the likely warmer and more turbulent periphery near or even into the TML. H I and O I have nearly identical ionization potential which leads to nearly identical ion fraction profiles, sampling points similarly along the line of sight, heavily weighted toward the self-shielded center of the cloud. As a result, we can use H I and O I to separate the thermal and turbulent components and be confident that the result reflects the mean along the line of sight, weighted heavily toward the center of the core and not affected significantly by the TML.

Using the velocity dispersion values for H I and O I from Table 3 and solving the above equations yields  $T = 8350 \pm 350$  K and turbulent dispersion  $\sigma_t = 5.3 \text{ km s}^{-1}$ , both of which are quite consistent with expectations for WNM/WIM. It is interesting to note that if we assume that Si II and C II are at this same temperature throughout the core column, their turbulent dispersion components come out to  $6.9 \text{ km s}^{-1}$  and  $8.9 \text{ km s}^{-1}$ , respectively. This is consistent with Si II, with its ionization potential higher than H I, surviving further into an increasingly turbulent periphery and C II, with an even higher potential, surviving further still into even higher turbulence as the WNM/WIM core transitions to the TML.

#### 4.3. Cloud Ionization

Our picture of the cloud is of a partially ionized stable WNM/WIM core, surrounded by a TML, in which diffuse WNM/WIM clumps are dispersed. These small, dispersed clumps are exposed to not only ionizing extragalactic and Galactic radiation, but are also embedded in the ionizing radiation produced locally by the collisional processes in the warmer phases of the TML. We therefore assume that the clumps are highly ionized and essentially transparent to Galactic UV and extragalactic background, which reaches the core at full strength. We now investigate whether a 3D photoionization model of the cloud core exposed to the Galactic and extragalactic UV radiation field can reproduce a neutral component consistent with our core model. We use a version of the 3D Hydrogen-only ionization equilibrium code of Wood & Loeb (2000). The code was set up to include a Galactic and extragalactic ionizing flux. A 3D spherical cloud of uniform volume density is discretized onto a linear Cartesian grid with 129 cells on a side. The gas is assumed to be isothermal, with recombination rates based on a kinetic temperature of 8000 K.

The gas can be made clumpy with a fractal-generated density modulation calculated using the algorithm of Elmegreen (1997) (as described in several papers *e.g.*, Mathis et al. 2002; Wood et al. 2005). This algorithm leaves a fraction of the gas as the smooth component and redistributes the remaining gas into hierarchical clumps. The fractal dimension  $f$  and parameters  $N_1$  through  $N_5$  govern the process. For more on these parameters and their effect on density structure, see the above-mentioned references. In this study, our purpose is only to include the general effect of clumpiness on the density profile shape for no other reason than to add some measure of realism to the cloud. It is not to emulate large-scale structure (the original purpose of this algorithm) nor any

particular ISM environment. We empirically adjusted the  $f_{smooth}$  and fractal parameters of the algorithm to produce, after ionization, only one distinct neutral structure representing the cloud core (with some parameter settings, there were two cores) while still producing distinct substructure. We settled on  $f_{smooth} = 0.85$ , fractal dimension  $f = 2.6$  with  $N_1$  through  $N_5$  set to 64, 16, 16, 16 and 16, respectively.

In order to demonstrate that photoionization alone can produce a neutral core consistent with our observations, we exposed a spherical cloud of uniform average density to ionizing radiation appropriate to our assumed distance of 70 kpc. A density of  $5.5 \times 10^{-3} \text{ cm}^{-3}$  was assumed which is somewhat higher than that of our core model (Table 2), thus allowing for a moderate ion fraction at the center. Again this is merely a demonstration illustrating what the actual profile, unresolved by our observations, might look like based on exposure to a realistic ionizing field. The ionization flux used is a combination of constant isotropic extragalactic ionizing background of  $7.9 \times 10^3 \text{ cm}^{-2} \text{ s}^{-1}$  from Faucher-Giguère et al. (2009)<sup>4</sup> and directional Galactic flux of  $1.3 \times 10^4 \text{ cm}^{-2} \text{ s}^{-1}$  from the model of Fox et al. (2005)<sup>5</sup> calculated at the cloud’s Galactic coordinates from Table 2 and assumed LOS distance of 70 kpc. The results are shown in Figure 9. To obtain the ionization results, we kept the density and fractal parameters constant and adjusted the cloud radius in order to obtain the observed central H I column density of  $N_c = 4.8 \times 10^{18} \text{ cm}^{-2}$  (Table 2) as measured along the Galactocentric LOS, defined in the local rectilinear coordinate system as the  $z$ -direction. When calculating average density profile and column density, the cloud center is determined from the 3D centroid of the neutral density distribution.

Figure 9(a) shows the resultant neutral density structure in the  $x - z$  plane after the cloud has reached ionization equilibrium. Figure 9(b) shows the cloud H I and total Hydrogen density profile through the centroid along the LOS. The photoionized cloud component is more extended than the neutral core. Note the asymmetry with the neutral core to right of center. This is due to the directional Galactic radiation component, providing increased flux along the LOS, which is aligned closely with Galactic Center. The remaining neutral core has a FWHM size of 319 pc. Figure 9(c) shows the average radial H I and total Hydrogen density profiles from the simulation. Also shown is our observation-based model core H I profile for comparison (from Table 2).

The neutral density profile (Figure 9(b)) of the ionized cloud core approximates a composite exponential profile dropping rapidly near the more neutral center and then a longer scale takes over as it becomes more ionized at larger radii. This is typical of ionization fronts, as in Zheng et al. (2002), where logarithmic plots show three slope regimes, a flat range if the core is fully shielded, followed by a steep region with moderate ionization and then a shallower one with high ionization. Since in our example the core is not fully shielded, there is no flat region. Our crude core model of constant density derived from observations approximates this more realistic

density profile as a constant, roughly equal to the central density truncated at about half the full extent of the core, which has a radius of 319 pc.

This photoionization model also provides information about the neutral fraction of the cloud. We calculate the neutral fraction from Figure 9(b) by comparing neutral and ionized hydrogen profiles and find a fraction of 24% along the central LOS. This is three times higher than 7% determined by FSW10 based on CLOUDY simulations for low ions. FSW10 also determined a lower limit for the incident ionization parameter,  $U = n_\gamma/n_H > 5 \times 10^{-4}$ . The equivalent  $U$  for our example is  $9.7 \times 10^{-5}$ , a factor of 5 lower. To get the FSW10 value of  $U$ , our simulations must be at an either unrealistically low or high distance ( $< 20$  kpc or  $> 200$  kpc) to get high enough Galactic  $n_\gamma$  or low enough  $n_H$ , respectively. Realistically, the ionizing flux and therefore  $U$  would be even lower if partial shielding of the extragalactic flux by the Galactic disk and the neighboring western complex were taken into account, increasing the discrepancy. Given the insight we now have into the structure along the NGC 7469 sight line, it can be argued that for the core and envelope structure we propose, FSW10’s CLOUDY analysis overestimates both  $U$  and the ion fraction for the low ion core environment. Their analysis used the total metal column densities, which include significant metal ion column density from envelope velocity components, as targets for the simulation. If these absorption components occur in highly ionized WIM fragments dispersed in the TML as we propose, their contributions would not be well represented as part of an integral CLOUDY slab model. Also, higher potential ions like Si II and C II would disproportionately sample warmer portions of the ambient collisional mixture. Furthermore, local TML collisional FUV radiation could contribute to the ionization state of the WIM fragments, further biasing the modeling results. It would be interesting to repeat the FSW10 simulations using only the metal column densities associated with the core velocity as targets. Given the high slopes in FSW10 Figure 5 (left) for the high potential ions, this could result in a significantly lower  $U$  and ion fraction more in line with our results.

In summary, we showed that we can reproduce the observed H I column density and the rough size of the cloud core relatively easily and with simple assumptions, in the scenario where the core represents the remnant of a larger cloud exposed to Galactic and extragalactic background ionizing radiation. The photoionization exercise also suggests that a large percentage (76% in this example) of the warm phase core of this cloud is ionized.

#### 4.4. Cloud Lifetime

If we assume that the mixing layer is merely a transport mechanism for the WNM/WIM of the cloud to ablate into the Halo, we can apply the hydrodynamic ablation equations of Pittard (2007) (pg. 245) to estimate the lifetime of the model cloud. In this calculation, we use the total estimated cloud mass from Table 2 which includes all warm phase gas (WNM or WIM) and the lifetime is the time required for all of this warm phase gas to be heated and absorbed into the hot Halo. This lifetime estimate will be on the high side since we are starting with the ablation process well underway with the warm envelope mass already in transition. It should be noted that

<sup>4</sup> Calculated from energy spectrum provided online by the authors at [www.cfa.harvard.edu/~cgiguere/UVB.html](http://www.cfa.harvard.edu/~cgiguere/UVB.html)

<sup>5</sup> From data kindly provided by Joss Bland-Hawthorn.

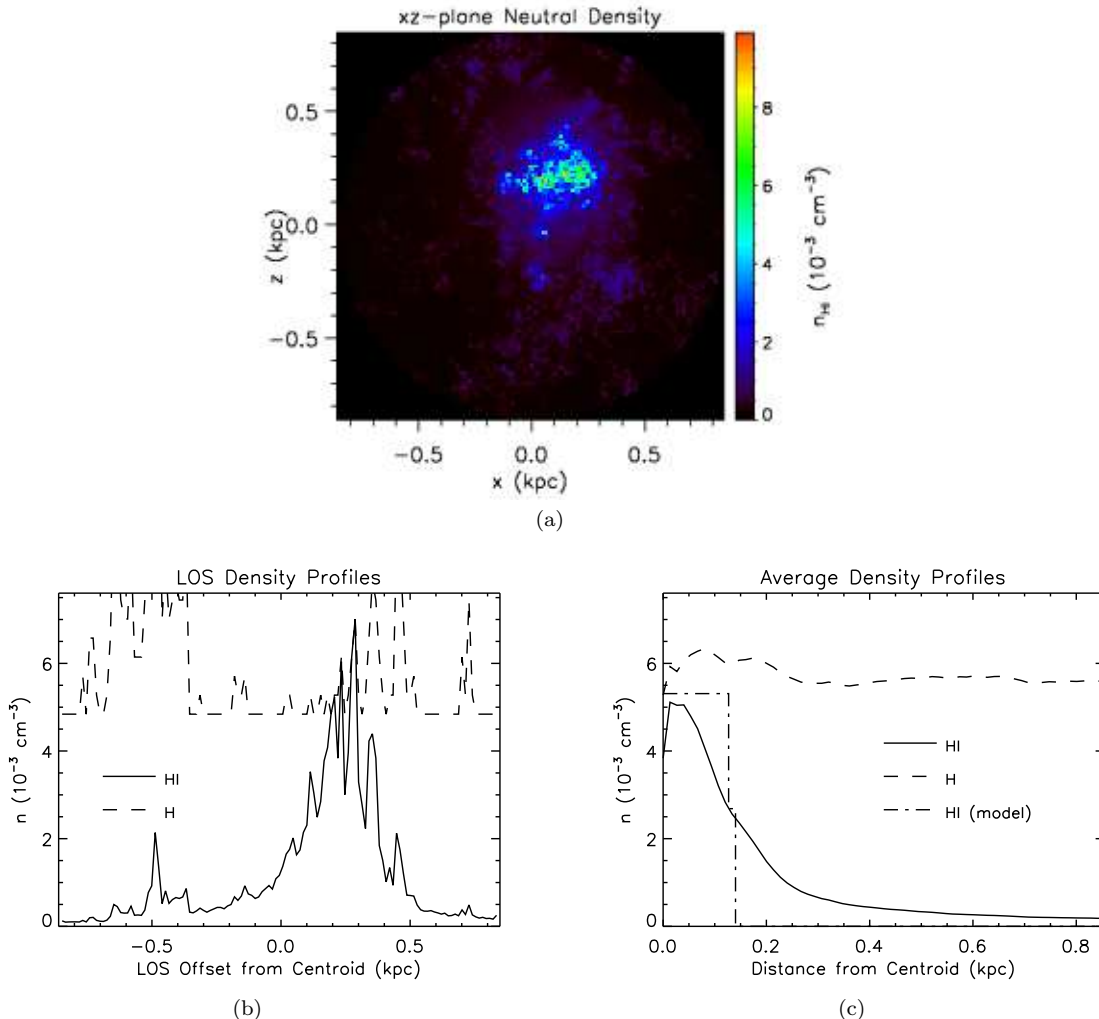


FIG. 9.— Neutral density characteristics of a 15% clumpy cloud core with uniform average density  $5.5 \times 10^{-3} \text{ cm}^{-3}$ , ionized 3D spherical cloud at Galactocentric distance 70 kpc exposed to standard Galactic and extragalactic ionizing radiation assuming the surrounding envelope is highly ionized and transparent. The cloud radius was adjusted to achieve the central column density of the cloud core observation-based model,  $N_{\text{HI}} = 4.8 \times 10^{18} \text{ cm}^{-2}$ . Plots for each case are (a) LOS neutral column density; (b) density profile along a LOS through the centroid; and (c) average radial density profile along with that from our model.

our averaging techniques expose a normally undetected envelope whose observed neutral mass is  $\approx 7$  times that of the core, so a very large portion of the mass of this cloud is in the envelope. This suggests that ablation time calculations based on cloud masses inferred from column densities of conventional HI maps will be quite low since the unobserved envelope may contain the majority of un-ablated mass.

Assuming a distance  $D = 70 \text{ kpc}$ , the total cloud mass estimate from Table 2 is  $M_c = 4 \times 10^5 M_\odot$ . We assume a peculiar cloud velocity of  $400 \text{ km s}^{-1}$  with respect to a non-rotating Halo ( $v_{\text{LOS}} = 350 \text{ km s}^{-1}$  plus some moderate proper motion), WNM/WIM cloud sound speed  $c_c \approx 10 \text{ km s}^{-1}$ , and Halo properties  $T_{\text{halo}} \approx 10^6 \text{ K}$ , and  $n_{\text{halo}} \approx 10^{-4} \text{ cm}^{-3}$  (Fang et al. 2006) on order of typically assumed values. The flow will be supersonic for these conditions, so we use  $\dot{M} = (M_c c_c)^{2/3} (\rho_{\text{halo}} v)^{1/3} \approx 3 \times 10^3 M_\odot \text{ Myr}^{-1}$  for a cloud lifetime of  $t_c \approx 140 \text{ Myr}$ . The infall distance prior to destruction is on order of  $v_{\text{LOS}} t_c = 50 \text{ kpc}$ , not quite surviving to the Galactic Disk from the assumed distance.

However, mass loss rates could be considerably lower due to factors not accounted for in the above equation such as recycling of WNM/WIM gas through rapid cooling (Begelman & Fabian 1990; Kwak et al. 2011), conduction effects (Vieser & Hensler 2007a) and magnetic fields (Esquivel et al. 2006).

Kwak et al. (2011) performed long term simulations of clouds with properties on the same order as ours except for an assumption of solar metallicity rather than the 0.1 solar estimate for this cloud (Fox et al. 2010). Their model “D” has comparable initial mass and retains 70% of its mass after 240 Myr. Its velocity is less than half that of ours, but the simulations and the authors’ analysis suggest that once supersonic, flow velocity has a large effect on cloud morphology, but little effect on the mass loss rate. These models suggest the cloud should have a lifetime as WNM/WIM on order of twice that calculated with the Pittard (2007) equation, long enough for it to potentially get within reach of the Galactic Disk. It should be pointed out that if cooling in the TML indeed slows ablation through recycling as mentioned above, the lower metallicity would reduce the lifetime by some un-

known amount.

On the other hand, Heitsch & Putman (2009) performed 3D simulations of clouds falling through the Halo assuming 0.1 solar abundances so cooling effects are appropriate to our cloud. They directly traced the smaller WNM/WIM clump fragments like those that compose our observed envelope. The cases illustrated are mostly subsonic at all times and clumps generally trail the core mass, but in one of the free-fall simulations shown, it briefly becomes transonic and develops some leading clumps suggesting that vortices are developing as they do in other supersonic simulations like Kwak et al. (2011). Their model “Wb1a15b” has initial mass  $3 \times 10^3 M_\odot$  and loses 50% of its mass to the Halo in 50 Myr (their Figure 3) and extrapolating to full mass loss, lasting  $\sim 100$  Myr. To estimate our cloud’s lifetime, we start with the integral core mass only (without the envelope) as this corresponds to the initial state of the simulations. We assume that the core will ablate similarly to the simulated cloud independent of a the pre-existing envelope. Our neutral core mass at 70 kpc is  $2.5 \times 10^3 M_\odot$  (Table 2) and allowing for 24% ionization as estimated in Section 4.3, is  $\sim 3\times$  the mass of the simulated cloud. The flow is Mach 0.7 in the simulation and so should ablate at nearly the same rate. The extrapolated lifetime of our cloud would be on order of 300 Myr, more than twice the Pittard (2007) calculation, and easily sufficient to reach the Disk with some WNM/WIM mass remaining.

In summary, the low-end estimate of cloud survival time as WNM/WIM prior to being subsumed by the Halo is 140 Myr, insufficient to reach the Galactic Disk. This is based on the analysis of Pittard (2007) which does not account for cooling or other factors that have been shown to suppress ablation. The numerical results of Kwak et al. (2011) which include cooling, suggest that the time to full destruction of warm gas in a similar cloud is much longer, by up to a factor of 2 or more although assumed solar metallicity puts this estimate on the high side. However, rough extrapolation of Heitsch & Putman (2009) simulations, with abundances appropriate to our cloud indicate that, at more than twice the Pittard (2007) lifetime, it is possible or even likely that warm gas will reach the Disk.

## 5. SUMMARY AND CONCLUSIONS

We have obtained deep H I 21 cm emission measurements mapping the vicinity of a relatively isolated, circularly projected cloud in the northern MS and applied a new spatial averaging technique to profile its mean spectrum vs. projected distance from the cloud center. Although near a larger cloud complex from which it appears to be separating, the cloud is well defined in angular extent and very well defined in velocity. By exploiting the approximate azimuthal symmetry of the cloud and averaging along successively larger concentric circular paths, we obtained correspondingly increased sensitivity without compromising the essential spatial resolution along the radial dimension. With this method, we detected and characterized core emission having  $\approx 20 \text{ km s}^{-1}$  WNM/WIM-like FWHM with velocity of  $\approx -340 \text{ km s}^{-1}$  and an envelope with broad diffuse emission having  $\approx 60 \text{ km s}^{-1}$  FWHM and velocity of  $\approx -360 \text{ km s}^{-1}$  extending well beyond the apparent periphery of the cloud’s emission. We then obtained

robust estimates of the core and envelope spectral properties by optimally matching the observed, averaged profile to a simple, spherical 3D core-plus-envelope emission model of the cloud projected on to the sky and averaged using the same method.

The envelope probes the neutral component of a boundary layer between the infalling WNM/WIM cloud core and the ambient HIM of the Halo. Assuming that the broad line width reflects very warm transition gas in a conductive boundary layer, we estimate the detected extent of the neutral envelope is more than an order of magnitude beyond what should be detectable based on the analyses and simulations of cloud evaporation. We conclude that a Turbulent Mixing Layer (TML) best explains the observed characteristics. Theoretical treatments and numerical simulations in the literature show that a TML has properties that can explain both the envelope line width and leading velocity where the envelope is composed of small clumps of narrower-width WNM/WIM dispersed over a large velocity range amidst warmer gas in the TML. This presents a wide Gaussian-like spectrum when a large number of these small clumps are within the beam with some leading and some lagging the core component. The leading clumps are also explained by the TML where vortices develop near the infalling core when flow is supersonic as expected and demonstrated in various numerical simulations.

Passing through the cloud and fortuitously near its center, is the NGC 7469 background source sight line which was characterized by FSW10 using optical and UV absorption data. Because O I and H I trace virtually identical profiles weighted toward the center of a partially photoionized cloud, we used measured velocity dispersions from FSW10’s O I and our H I core velocity components to establish a core temperature  $T = 8350 \pm 350 \text{ K}$  with a turbulent component  $\sigma_t = 5.3 \text{ km s}^{-1}$ , consistent with WNM/WIM.

The role of photoionization on the cloud was investigated using a 3D photoionization equilibrium program. Assuming that the collisionally ionized warm TML gas as well as the interspersed WNM/WIM clumps are highly ionized, we treated the envelope as transparent to Galactic and extragalactic ionizing radiation. We exposed a clumpy spherical cloud with radius 320 pc at a distance of 70 kpc with uniform average Hydrogen density of  $5.5 \times 10^{-3} \text{ cm}^{-3}$  to combined Galactic and extragalactic ionizing flux based on published values at this distance. We determined that the centrally concentrated exponential profile of the neutral component is approximated well by our simple uniform neutral density model of  $\sim 1/2$  the radius. The core’s actual extent as WNM/WIM is therefore on order of twice that of our 3D neutral component model. The neutral fraction along the central LOS is 24% and the ionization parameter is  $9.7 \times 10^{-5}$ , quite different from FSW10’s estimates of 7% and  $> 5 \times 10^{-4}$ , respectively. We are unable to approach FSW10’s values with any realistic cloud at a realistic distance. We conjecture that the discrepancy is at least partially due to FSW10’s inclusion of what we suggest are envelope velocity components in abundance calculations. If produced in the clumpy, warmer and partially collisional envelope environment we propose, these components would not be represented well by CLOUDY.

The cloud lifetime assuming simple hydrodynamic ablation driven by shear instability in supersonic flow is estimated at  $\sim 140$  Myr, insufficient for any WNM or WIM to reach the Disk and potentially fuel future star formation. However, a TML is expected to partially suppress ablation through re-cooling of some of the heated gas (Begelman & Fabian 1990). Simulation of a comparable infalling cloud by Kwak et al. (2011) which includes cooling indicates a dramatically increased  $\sim 2\times$  lifetime, suggesting that a large portion of the total mass could reach the disk. This result is supported by extrapolating the simulations of Heitsch & Putman (2009).

Through our use of the spatial averaging technique, this work provides the first look (or more accurately, a peek) at the structure of the highly ionized and diffuse boundary layer between the warm neutral gas of the MS and the HIM of the Halo from the perspective of the low temperature side of the interface. FSW10 provides a rich set of data and analysis for the fortuitously aligned NGC 7469 sight line, creating a mini-laboratory to study MS-Halo interaction. We were able to incorporate some of their results to complement ours, but were unable to quantify characteristics of the barely probed TML. To fully exploit this alignment of complementary data, hydrodynamic simulations that emulate the evolution of the larger environment of the cloud (*i.e.*, including the neighboring cloud complex) would be needed that allow simulated observations on a similar cloud feature. Photoionization would have to be accounted for and its possible impact on the hydrodynamic evolution would have to be addressed.

Future work will include applying the technique to isolated circular or filamentary structures (with or without

benefit of well-placed background sources) in other parts of the MS, both upstream and downstream to see if this apparent mixing layer is common and if its characteristics vary with time, indicated by the location along the MS. We also plan to obtain higher resolution maps on this cloud and others with the Arecibo Telescope to complement the lower resolution GBT data and gain insight into the smaller scale structure. Further in the future, we plan to apply the technique to deep, very high resolution observations of such clouds using a large array such as the Australian Square Kilometre Array Pathfinder (ASKAP).

It is our pleasure to thank Felix J. Lockman for his support in observations, data reduction and interpretative discussions. We also thank Andrew Fox, Joss Bland-Hawthorn, Bart Wakker, Jennifer Stone, Ellen Zweibel, Alex Hill, Matt Haffner and Kelley Hess for stimulating discussions as well as the anonymous referee for useful comments leading to improvements to the paper. We acknowledge support by the NSF through grants AST-0908134 and AST-708967. LN thanks the Arecibo Observatory for a pre-doctoral fellowship. SS acknowledges support by the Research Corporation for Science Advancement. The Arecibo Observatory is operated by SRI International under a cooperative agreement with the National Science Foundation (AST-1100968), and in alliance with Ana G. Méndez-Universidad Metropolitana, and the Universities Space Research Association. The National Radio Astronomy Observatory is a facility of the National Science Foundation operated under cooperative agreement by Associated Universities, Inc.

*Facilities:* GBT.

## REFERENCES

- Agertz, O., et al. 2007, MNRAS, 380, 963  
 Begelman, M. C., & Fabian, A. C. 1990, MNRAS, 244, 26P  
 Besla, G., Kallivayalil, N., Hernquist, L., Robertson, B., Cox, T. J., van der Marel, R. P., & Alcock, C. 2007, ApJ, 668, 949  
 Besla, G., Kallivayalil, N., Hernquist, L., van der Marel, R. P., Cox, T. J., & Kereš, D. 2010, ApJ, 721, L97  
 Bland-Hawthorn, J., Sutherland, R., Agertz, O., & Moore, B. 2007, ApJ, 670, L109  
 Bland-Hawthorn, J. 2009, IAU Symposium, 254, 241  
 Brooks, A. M., Governato, F., Quinn, T., Brook, C. B., & Wadsley, J. 2009, ApJ, 694, 396  
 Brüns, C., Kerp, J., & Pagels, A. 2001, A&A, 370, L26  
 Brüns, C., et al. 2005, A&A, 432, 45  
 Collins, J. A., Shull, J. M., & Giroux, M. L. 2009, ApJ, 705, 962  
 Connors, T. W., Kawata, D., & Gibson, B. K. 2006, MNRAS, 371, 108  
 Cowie, L. L., & McKee, C. F. 1977, ApJ, 211, 135  
 Dalton, W. W., & Balbus, S. A. 1993, ApJ, 404, 625  
 Dekel, A., & Birnboim, Y. 2006, MNRAS, 368, 2  
 Draine, Bruce T. 2011, Physics of the Interstellar and Intergalactic Medium (Princeton, NJ, USA: Princeton University Press)  
 Elmegreen, B. G. 1997, ApJ, 477, 196  
 Esquivel, A., Benjamin, R. A., Lazarian, A., Cho, J., & Leitner, S. N. 2006, ApJ, 648, 1043  
 Fang, T., Mckee, C. F., Canizares, C. R., & Wolfire, M. 2006, ApJ, 644, 174  
 Faucher-Giguère, C. A., Lidz, A., Zaldarriaga, M., & Hernquist, L. 2009, ApJ, 703, 1416  
 Fisher, J. R., Norrod, R. D., & Balsaer, D. S. 2003 GBT Electronics Division Internal Report No. 312, <http://www.gb.nrao.edu/electronics/edir/index.html>  
 Fox, A. J., Wakker, B. P., Savage, B. D., Tripp, T. M., Sembach, K. R., & Bland-Hawthorn, J. 2005, ApJ, 630, 332  
 Fox, A. J., Wakker, B. P., Smoker, J. V., Richter, P., Savage, B. D., & Sembach, K. R. 2010, ApJ, 718, 1046  
 Gallagher, J. S., & Smith, L. J. 2005, Extra-Planar Gas, 331, 147  
 Gnat, O., Sternberg, A., & McKee, C. F. 2010, ApJ, 718, 1315  
 Heitsch, F., & Putman, M. E. 2009, ApJ, 698, 1485  
 Hilditch, R. W., Howarth, I. D., & Harries, T. J. 2005, MNRAS, 357, 304  
 Jin, S., & Lynden-Bell, D. 2008, MNRAS, 383, 1686  
 Kalberla, P. M. W., & Haud, U. 2006, A&A, 455, 481  
 Kereš, D., Katz, N., Weinberg, D. H., & Davé, R. 2005, MNRAS, 363, 2  
 Koerwer, J. F. 2009, AJ, 138, 1  
 Kwak, K., Henley, D. B., & Shelton, R. L. 2011, ApJ, 739, 30  
 Mastropietro, C., Moore, B., Mayer, L., Wadsley, J., & Stadel, J. 2005, MNRAS, 363, 509  
 Mathis, J. S., Whitney, B. A., & Wood, K. 2002, ApJ, 574, 812  
 McClure-Griffiths, N. M., et al. 2009, ApJS, 181, 398  
 McKee, C. F., & Cowie, L. L. 1977, ApJ, 215, 213  
 Moore, B., & Davis, M. 1994, MNRAS, 270, 209  
 Mori, M., & Burkert, A. 2001, The Physics of Galaxy Formation, 222, 359  
 Nidever, D. L., Majewski, S. R., & Burton, W. B. 2008, ApJ, 679, 432  
 Nidever, D. L., Majewski, S. R., Butler Burton, W., & Nigra, L. 2010, ApJ, 723, 1618  
 Nelder and Mead, 1965, Computer Journal, Vol 7, pp 308-313.  
 Pittard, J. M. 2007, in Diffuse Matter from Star Forming Regions to Active Galaxies, ed. T. W. Hartquist et al. (Dordrecht, The Netherlands: Springer)

- Putman, M. E., Staveley-Smith, L., Freeman, K. C., Gibson, B. K., & Barnes, D. G. 2003, *ApJ*, 586, 170
- Putman, M. E., Bland-Hawthorn, J., Veilleux, S., Gibson, B. K., Freeman, K. C., & Maloney, P. R. 2003, *ApJ*, 597, 948
- Quilis, V., & Moore, B. 2001, *ApJ*, 555, L95
- Reynolds, R. J., Tufte, S. L., Haffner, L. M., Jaehnig, K., & Percival, J. W. 1998, *PASA*, 15, 14
- Sembach, K. R., et al. 1995,
- Sembach, K. R., et al. 2003, *ApJS*, 146, 165
- Shull, J. M., Jones, J. R., Danforth, C. W., & Collins, J. A. 2009, *ApJ*, 699, 754
- Silk, J., Wyse, R. F. G., & Shields, G. A. 1987, *ApJ*, 322, L59
- Slavin, J. D., Shull, J. M., & Begelman, M. C. 1993, *ApJ*, 407, 83
- Spitzer, Lyman, Jr. 1998, *Physical Processes in the Interstellar Medium* (Berlin, DE: Wiley-VCH)
- Stanimirović, S., Dickey, J. M., Krčo, M., & Brooks, A. M. 2002, *ApJ*, 576, 773
- Stanimirović, S., Hoffman, S., Heiles, C., Douglas, K. A., Putman, M., & Peek, J. E. G. 2008, *ApJ*, 680, 276
- Stanimirovic, S., Gallagher, J. S., III, & Nigra, L. 2010, *Serbian Astronomical Journal*, 180, 1
- Tüllmann, R., Pietsch, W., Rossa, J., Breitschwerdt, D., & Dettmar, R.-J. 2006, *A&A*, 448, 43
- Vieser, W., & Hensler, G. 2007a, *A&A*, 472, 141
- Vieser, W., & Hensler, G. 2007b, *A&A*, 475, 251
- Wakker, B. P., York, D. G., Wilhelm, R., et al. 2008, *ApJ*, 672, 298
- Weiner, B. J., & Williams, T. B. 1996, *AJ*, 111, 1156
- Wolfire, M. G., McKee, C. F., Hollenbach, D., & Tielens, A. G. G. M. 1995, *ApJ*, 453, 673
- Wood, K. & Loeb, A. 2000, *ApJ*, 545, 86
- Wood, K., Haffner, L. M., Reynolds, R. J., Mathis, J. S., & Madsen, G. 2005, *ApJ*, 633, 295
- Zheng, Z., & Miralda-Escudé, J. 2002, *ApJ*, 568, L71